EUROPEAN ORGANIZATION FOR NUCLEAR RESEARCH

MEASUREMENT OF THE Σ^0 LIFETIME[†)]

F. Dydak, F.L. Navarria[*)], O.E. Overseth[**)], P. Steffen[+)],
J. Steinberger, H. Wahl and E.G.H. Williams
CERN, Geneva, Switzerland

F. Eisele, C. Geweniger and K. Kleinknecht
Institut für Physik der Universität Dortmund, Germany

H. Taureg and G. Zech[++)]
Institut für Hochenergiephysik der Universität Heidelberg, Germany

ABSTRACT

The Coulomb production of Σ^0 hyperons on uranium and nickel nuclei has been measured in a beam of Λ hyperons at the CERN Proton Synchrotron. The results for the Σ^0 lifetime, $\tau_{\Sigma^0} = (0.58 \pm 0.13) \times 10^{-19}$ sec, and for the Σ^0-Λ magnetic transition moment, $|\mu_{\Sigma\Lambda}| = (1.90 \,^{+\,0.26}_{-\,0.19})$ nuclear magnetons, are in agreement with SU(3) predictions.

Geneva - 25 August 1976
(Submitted to Nuclear Physics B)

---

†) Work supported in part by Bundesministerium für Forschung und Technologie, Bonn, Germany.

*) On leave from the Istituto di Fisica dell'Università, Bologna, Italy.

**) On leave from the University of Michigan, Ann Arbor, Michigan, USA.

+) Now at DESY, Hamburg, Germany.

++) Now at Gesamthochschule Siegen, Siegen, Germany.

1. INTRODUCTION

The dominant decay mode of the Σ^0 hyperon is $\Sigma^0 \to \Lambda + \gamma$, and its lifetime is determined by the Σ^0-Λ magnetic transition moment $\mu_{\Sigma\Lambda}$. Within the framework of SU(3), the magnetic moments of the members of the baryon octet and the magnetic transition moment $\mu_{\Sigma\Lambda}$ are related to the neutron and proton magnetic moments μ_n and μ_p, respectively.

In particular, one gets [1]

$$\mu_{\Sigma\Lambda} = -\frac{\sqrt{3}}{2}\mu_n = 1.66\,\frac{e\hbar}{2m_p c}\,. \tag{1}$$

With this prediction one calculates a Σ^0 lifetime of

$$\tau_{\Sigma^0} = \frac{\pi}{k^3}\,\frac{m_{\Sigma^0}}{E_\Lambda}\,\frac{1}{\mu^2_{\Sigma\Lambda}} = 0.76 \times 10^{-19}\ \text{sec}\,, \tag{2}$$

where k denotes the photon momentum in the Σ^0 rest frame, m_{Σ^0} the Σ^0 mass, and E_Λ the Λ energy in the Σ^0 rest frame [2].

This lifetime is too short to be observed directly from a decay length distribution with present techniques. Only an experimental upper limit of $\tau_{\Sigma^0} < 1.0 \times 10^{-14}$ sec has been determined [3]. A measurement of τ_{Σ^0} from the mass width is impossible at present since the predicted width $\Gamma = 8.6$ keV is too small.

However, an indirect determination of the Σ^0 lifetime is feasible via a measurement of the Coulomb production cross-section of the reaction (Fig. 1)

$$\Lambda + (Z) \to (Z) + \Sigma^0\,,$$

where (Z) stands for the Coulomb field of a nucleus. The measurement of this process, commonly known as the Primakoff effect, was independently proposed in 1961 by Dreitlein and Primakoff [4], Williams, and Pomeranchuk and Shmushkevitch [5]. Its differential cross-section is described by the formula:

$$\frac{d\sigma}{dq_t^2} = 70\pi\left(\frac{Z}{82}\right)^2\left(\frac{10^{-19}\ \text{sec}}{\tau_{\Sigma^0}}\right)\frac{p_\Lambda^2}{m_\Lambda^4}\left[\frac{q_\ell q_t}{q_\ell^2 + q_t^2}\,F(\vec{q})\right]^2\frac{\text{mb}}{(\text{GeV/c})^2} \tag{3}$$

where

Z = charge of the target nucleus,

p_Λ = momentum of the incident Λ,

$q_\ell \simeq (m^2_{\Sigma^0} - m^2_\Lambda)/2p_\Lambda$ = longitudinal momentum transfer,

$q_t = p_\Lambda \sin\theta \simeq p_\Lambda\,\theta$ = transverse momentum transfer,

$F(\vec{q})$ = form factor of the nucleus as a function of the momentum transfer $\vec{q}$, and

$q^2 = \vec{q}^2 = q^2_\ell + q^2_t \approx q^2_t$ for Λ momenta of several GeV/c, and small scattering angles θ.

The Coulomb production cross-section (3) is characterized by the following properties:

i) $d\sigma/dq^2_t$ vanishes at $q_t = 0$, rises to a sharp peak at $q^2_t \simeq \left[(m^2_{\Sigma^0} - m^2_\Lambda)/2p_\Lambda\right]^2$, and falls off approximately like an exponential with a slope parameter ranging from 2200 $(GeV/c)^{-2}$ to 3700 $(GeV/c)^{-2}$ for incident Λ momenta p_Λ between 10 and 20 GeV/c. This property, in particular, makes it possible to distinguish Coulomb production from strong coherent production processes which show a much weaker fall-off. For comparison, the diffraction slope parameter on uranium [6] is 350 $(GeV/c)^{-2}$.

ii) The total Coulomb production cross-section rises with the incident Λ momentum approximately as $\log p_\Lambda$. Therefore the highest available momenta give the best discrimination against competing strong coherent Σ^0 production, which is expected to fall with p_Λ.

iii) The Coulomb production yield is nearly independent of Z, if one uses targets of the same thickness in terms of radiation lengths. However, the discrimination against strong production is, in general, better for heavy nuclei such as uranium.

The main problem in the isolation of the Primakoff process usually is its possible interference with strong coherent production. It is important to note that in the process under consideration, that is the Λ-Σ^0 transition, only the $\Delta I = 1$ exchange mechanisms can contribute to the strong coherent amplitude. Therefore, its amplitude is expected to be proportional to the nuclear isospin $\frac{1}{2}(N - Z)$.

In this process the amplitude of the potentially dangerous coherent nuclear background is smaller by a factor (N - Z)/A compared to the case $\Delta I = 0$ contributing to the $\gamma \to \pi^0$ and $\gamma \to \eta^0$ Primakoff effect [7]. An isoscalar target is therefore advantageous. As a result of this, we have chosen besides a uranium target (Z = 92, N - Z = 54) also a nickel target (Z = 28, N - Z = 2.7).

Wilkin [8] has calculated the Coulomb production cross-section using a parametrization of the nuclear form factor $F(\vec{q})$ derived from elastic-scattering data of electrons on nuclei, and taking into account the absorption of both the incoming and the outgoing hyperons as described by Fäldt [9]. Whereas the detailed form of the nuclear form factor is unimportant, because of the confinement of the Primakoff process to the very forward direction, the nuclear absorption correction reduces the cross-section by about 40% for uranium, and about 13% for nickel.

The present paper is subdivided as follows: In Section 2 we describe our experimental set-up. In Section 3 we describe the selection of $\Lambda \to p\pi^-$ events used to monitor the Λ flux and the selection of $\Sigma^0 \to \Lambda\gamma$ candidates. In Section 4 the analysis of the $\Sigma^0 \to \Lambda\gamma$ decays and the determination of the Coulomb production cross-section are described. Finally, in Section 5 we compare our result with theoretical predictions.

2. EXPERIMENTAL SET-UP

The experiment has been performed in a short-lived neutral beam at the CERN Proton Synchrotron (PS), providing Λ hyperons in the momentum range 5-20 GeV/c. The main elements of the set-up are shown in Fig. 2. They consist of a large-aperture magnetic spectrometer and a lead-glass array for the detection of photons and electrons. The spectrometer is a shortened version of the one used by the same group for the measurement of the decay parameters of the CP violating K^0 decay. Details have been given elsewhere [10], and here we will recall only its most important properties.

2.1 The magnetic spectrometer

Neutral hadrons are produced by an external proton beam of 24 GeV/c hitting a 4×4 mm^2 platinum target. The secondaries are selected at an average angle of 75 mrad by a tapered uranium collimator, 1.90 m long, which is embedded in a magnetic field of 20 kG in order to sweep out charged particles. A platinum absorber of a thickness of 12 radiation lengths behind the proton target removes the photons from the neutral beam. The target for the Λ-Σ^0 conversion ($6 \times 6 \times 0.6$ cm^3 uranium and $6 \times 6 \times 2$ cm^3 nickel, respectively) is placed at the collimator exit, 2.17 m from the proton target. It is followed by an anticounter and a 2.50 m long evacuated decay region. The produced Σ^0 hyperons are detected by their decay mode $\Sigma^0 \rightarrow \Lambda + \gamma$, whereas the Λ hyperons are detected by their charged decay mode $\Lambda \rightarrow p + \pi^-$.

The vector momenta of the proton and pion from the Λ decay are measured in a spectrometer consisting of four large multiwire proportional chambers and a bending magnet. All chambers are equipped with a horizontal and a vertical signal plane, each divided electronically into a left and a right half (the horizontal wires are cut in the middle and connected to amplifiers on either side). The wire spacing is 2 mm. The volume between the chambers is filled with helium to minimize multiple scattering.

A 2.5 m long threshold Čerenkov counter filled with methane at atmospheric pressure discriminates between electrons and pions up to a momentum of 4.8 GeV/c. The 270×140 cm^2 cross-section is subdivided by focusing mirrors into 12 optically independent cells, 6 above and 6 below the beam line, in order to identify electron tracks.

Muons with momenta above 1.45 GeV/c penetrate a 2.8 m long concrete shield and are identified in a scintillator hodoscope.

A 2×6 matrix of scintillation counters behind the last multiwire proportional chamber is used as a trigger counter. A right-left coincidence in this plane is required to initiate an event trigger.

2.2 The lead-glass detector

A large lead-glass hodoscope, covering an area of 1.8 m^2 is placed behind the trigger plane (see Fig. 2). It consists of 84 identical lead-glass blocks of the SF5 type (density 4.08 g/cm^3, index of refraction 1.67, radiation length 2.36 cm), each 14.6 × 14.6 × 30 cm^3. The depth of the lead-glass is 12.7 radiation lengths, containing 94% of a 1 GeV photon shower [11]. The blocks are assembled in two units, each comprising 6 rows and 7 columns. A 5 in. phototube is glued onto each block, and the anode signals are digitized in parallel by 84 ADCs.

The electromagnetic shower sometimes spreads over adjacent blocks. Therefore, the signals of the last dynodes of all counters forming adjacent columns are added linearly. A common threshold is set to a shower energy of about 0.6 GeV, well above the pulse height of 0.35 GeV produced by muons and hadrons. The timing of the standard signal outputs indicating pulse heights above the threshold is provided by a high-low coincidence circuitry thus allowing for a time resolution of 6 nsec FWHM in coincidence with the trigger counter. In the case where the lead-glass pulse height is in coincidence with the fast trigger within a gate width of 16 nsec, special "dynode bits" are set, labelling the respective lead-glass column. These bits are used in the off-line analysis, and enable an efficient rejection against accidental pulse heights recorded during the 150 nsec gate width of the ADCs.

Electrons and positrons originating mainly from K_{e3} decays are used for the continuous calibration. Their momenta are measured in the magnetic spectrometer, and are compared with the pulse heights obtained in the lead-glass detector. The energy resolution is about $\Delta E/E = 0.11/\sqrt{E(GeV)}$ FWHM and the shower position is determined from the pulse heights in adjacent blocks with an accuracy of σ = 2.7 cm.

Details of the lead-glass detector have been described elsewhere [12].

2.3 The trigger

A fast trigger was provided by a left-right coincidence of the trigger counter plane. A more refined decision is based on the requirement of exactly two hits per

wire chamber. Events with a signal from the anticounter are rejected. In addition, we require a signal above the lead-glass threshold. This last requirement is released for each 128th trigger, in order to record also events without photons for monitoring purposes. Such events are labelled with a "monitor bit", and are used for the determination of the Λ-flux.

Two different sets of data have been taken in three different running periods: two periods with a uranium target and a photon energy threshold of $\sim$ 0.6 GeV, and one period with a nickel target and a photon energy threshold of $\sim$ 0.8 GeV. The total running time was of the order of 600 h.

3. EVENT SELECTION AND ACCEPTANCE

3.1 $\Lambda \to p\pi^-$ selection and acceptance

Λ particles emerging from the proton target have to satisfy the following criteria:

i) The event must be labelled with a "monitor bit", i.e. it has been recorded irrespective of whether or not there was a pulse height in the lead-glass counter.

ii) Geometrical cuts select two charged tracks with opposite charge and straight horizontal track projections, originating from a common vertex within a few millimetres.

iii) Λ-decay candidates are selected by requiring a momentum asymmetry $(p_+ - p_-)/(p_+ + p_-) > 0.45$.

iv) The invariant mass $m(p,\pi^-)$ is required to differ from the Λ mass (1.1156 GeV/c^2) by less than 7 MeV/c^2, the Λ-mass resolution being σ = 1.5 MeV/c^2 (see Fig. 3).

v) The π^- momentum is required to exceed 1.2 GeV/c.

vi) The muon counter hodoscope is required to have no hit.

vii) The proper time from the Primakoff target to the decay vertex is required to be greater than 0.1×10^{-10} sec, and less than 4×10^{-10} sec.

viii) To select Λ's pointing back to the target, a cut $R_\Lambda^2 < 0.5$ cm^2 is applied, R_Λ^2 being the squared distance of the Λ trajectory from the proton target centre.

The invariant (p,π^-) mass distribution of the Λ events is shown in Fig. 3. The R_Λ^2 distribution is shown in Fig. 4. Both plots demonstrate a clean Λ signal, with a negligible background.

The momentum distribution of the accepted Λ events is shown in Fig. 5. It ranges from 5 to 21 GeV/c, with a maximum at 12 GeV/c.

The acceptance of the Λ decays has been determined by a Monte Carlo simulation. It is shown in Fig. 6 as a function of the momentum. For low momenta the acceptance is poor, since the relatively slow π^- is swept out by the bending magnet.

3.2 $\Lambda + \gamma$ event selection and acceptance

$\Lambda + \gamma$ events have to satisfy the following criteria:

i) Λ particles are selected by the same criteria (ii) to (vii) as applied to select Λ's emerging from the proton target (see Section 3.1).

ii) A cut $R_\Lambda^2 > 0.4$ cm^2 strongly suppresses transmitted Λ's accompanied by an accidental photon.

iii) Each energy cluster larger than 0.6 GeV in the lead-glass detector is called a photon if it has a distance of at least 15 cm from both charged tracks. The photon is only accepted if the respective "dynode bit" is set. We select Λ's associated with one such photon, with a photon energy of more than 0.8 GeV for the uranium data, and of more than 1.0 GeV for the nickel data, in order to exceed the hardware thresholds of 0.6 GeV and 0.8 GeV, respectively.

All cuts have been applied to the data as well as to the $\Sigma^0 \to \Lambda + \gamma$ decays generated by our Monte Carlo program. The Σ^0 acceptance is shown in Fig. 7 as a function of the momentum. It is rather independent of q^2 over the whole range of q^2 $[0 < q^2 < 0.01$ (GeV/c)$^2]$ covered in the further analysis.

In Fig. 8 we show the photon energy spectrum of accepted Σ^0 decays, as well as the efficiency of the "dynode bit" setting as a function of the photon energy. Above 0.8 GeV photon energy [cut (iii)] event losses due to inefficiencies are negligible.

In order to determine the experimental resolution of the Σ^0 production angle, we generate, using Monte Carlo techniques, Σ^0 hyperons at zero degrees with respect to the incoming Λ. The q^2 distribution obtained is shown in Fig. 9 for different Σ^0 momenta. We deduce an experimental resolution of about σ = 1.5 mrad in the Σ^0 production angle.

4. ANALYSIS OF $\Sigma^0 \to \Lambda + \gamma$ CANDIDATES

4.1 The cross-section for Σ^0 forward production

The distribution of the invariant mass $m(p,\pi^-)$ of the selected $\Lambda + \gamma$ events demonstrates that the Λ decay is unambiguously identified (Fig. 10). The background due to other V^0 decays is negligible.

The Σ^0-decay vertex is obtained from the intersection of the reconstructed Λ trajectory with the plane of the Primakoff target. Using the centre of the proton target, the direction of the incident Λ is determined with an accuracy of σ = 1.2 mrad. The photon direction is defined by the line from the centre of the energy cluster in the lead-glass detector to the Σ^0-decay vertex.

The resulting distribution of the invariant mass $m(\Lambda,\gamma)$ shows no peak at the Σ^0 mass (1.192 GeV/c^2) indicating Σ^0 production (Fig. 11). The distribution is dominated by $\Xi^0 \to \Lambda\pi^0$ decays, where only one photon from the π^0 decay is detected. However, if we restrict the events to higher $(\Lambda + \gamma)$ momenta ($13 < p_{\Lambda\gamma} < 19$ GeV/c) and to very small values of q^2 [$q^2 < 0.001$ (GeV/c)^2], we obtain an unambiguous signal from Σ^0 production in the mass distribution (Fig. 12a for uranium events, Fig. 13a for nickel events). No signal of Σ^0 production can be seen outside this small q^2 region, as shown in Figs. 12b and c and 13b and c, where the mass distribution $m(\Lambda,\gamma)$ is plotted for the regions $0.001 < q^2 < 0.002$ and $0.002 < q^2 < 0.004$ (GeV/c)^2, both for uranium and nickel data.

In order to study the Σ^0 production and the background shape in more detail, we select the events in five mass bins of 30 MeV/c^2, ranging from 1.115 to 1.265 GeV/c^2, and display their q^2 distribution (Figs. 14 and 15). In both cases, at low q^2 a clear signal above a rather flat background is found in the Σ^0 mass bin $[1.175 < m(\Lambda,\gamma) < 1.205$ GeV/$c^2]$, whereas no such forward peak exists in the adjacent mass bins.

The background in the q^2 distribution again can be understood in terms of $\Xi^0 \to \Lambda\pi^0$ decays with one undetected photon, and Λ's associated with one accidental photon. The q^2 distributions of Monte Carlo generated background events of this type are shown in Fig. 16. The background is smooth in the region of the Primakoff signal.

In Figs. 17 and 18 we present once more the q^2 distribution of the Σ^0 mass bin, showing the clear peak at low q^2 both for uranium (Fig. 17) and nickel data (Fig. 18).

The Σ^0 production at low q^2 can be understood in terms of the Primakoff effect alone, the q^2 distribution of which is displayed in Figs. 17 and 18 as a dashed histogram. No other production mechanism can give a fall-off with q^2 as steep as the measured distribution. Even the differential cross-section of diffraction scattering [slope parameter 350 $(GeV/c)^{-2}$ on uranium and 180 $(GeV/c)^{-2}$ on nickel, respectively] shows a much weaker fall-off than the experimentally observed q^2 distribution. Unfolding the experimental resolution we get a fall-off of about exp $(-3000\ q^2)$ as expected for Coulomb production. We conclude that the observed signal is predominantly due to Primakoff production.

The number of Σ^0 events in the mass range $1.175 < m(\Lambda,\gamma) < 1.205$ GeV/c^2 is obtained by an exponential background subtraction in the q^2 distribution. The data are binned in momentum intervals of 2 GeV/c. The subtraction is done in each bin separately. The signal region is confined to $q^2 < 0.001$ $(GeV/c)^2$, whereas the regions $0.002 < q^2 < 0.005$ $(GeV/c)^2$ and $0.005 < q^2 < 0.008$ $(GeV/c)^2$ are used for the background calculation. The background fit is indicated in Figs. 17 and 18 by smooth curves.

From the number of events after background subtraction, we calculate the cross-section for Σ^0 production according to

$$\sigma = \frac{N_{\Sigma^0}}{128 \times N_\Lambda} \frac{\alpha_\Lambda}{\alpha_{\Sigma^0}} \frac{A}{L} \frac{1}{\ell\left[1 - \exp\left(-d/\ell\right)\right]} \qquad (4)$$

where

N_{Σ^0} = number of Σ^0 events after the background subtraction

N_Λ = number of Λ monitor events (to be multiplied by a scaling factor 128; see Section 2.3)

α_Λ = acceptance of Λ events

α_{Σ^0} = acceptance of Σ^0 events produced by the Primakoff effect

A = atomic number of the Primakoff target (A = 238.1 for uranium, A = 58.7 for nickel)

L = Avogadro's number (6.022×10^{23} atoms/mole)

ℓ = $^9/_7$ ℓ_{rad}, where ℓ_{rad} denotes the radiation length (ℓ_{rad} = 6.07 g/cm^2 for uranium, ℓ_{rad} = 12.62 g/cm^2 for nickel)

d = target thickness (d = 11.4 g/cm^2 for uranium, d = 17.8 g/cm^2 for nickel).

The last term in formula (4) includes a correction for Σ^0 decays, where the photon is converted within the Primakoff target into electrons which are vetoed by the anticounter.

In Table 1 we list the number of Σ^0 events in different momentum bins and the respective cross-sections for uranium and nickel separately. The experimental cross-sections are consistent with a logarithmic rise with increasing ($\Lambda + \gamma$) momentum (Fig. 19), as expected for Primakoff production. This confirms the previous conclusion that the observed Σ^0 events originate predominantly from Coulomb production.

Possible systematic errors in the acceptance of the Λ decay would cancel in first order in formula (4), because they affect the Λ-monitor events in the same way as the Σ^0 events. Systematic errors in the photon acceptance are negligible compared to the statistical errors of the quoted Σ^0 event numbers.

In order to estimate the dependence of the quoted cross-sections on the method of background subtraction, a linear background subtraction has also been made as well as variations of the background regions. The cross-sections do not change significantly.

4.2 Upper limit for an interference with strong coherent Σ^0 production

A source of a systematic error could be the strong coherent Σ^0 production. Because the Λ-Σ^0 transition changes the isospin by one unit ($\Delta I = 1$), the process is expected to be dominated by π^0 and ρ^0 exchange. Theoretical estimates lead to negligible cross-sections [4,13]. In addition, an experimental upper limit for the cross-section of strong coherent Σ^0 production can be determined from our data as follows.

First of all, we note that there is no indication for a Σ^0 signal in the distribution of the mass $m(\Lambda,\gamma)$ in the q^2 bin $0.002 < q^2 < 0.004$ $(GeV/c)^2$, either for the uranium or for the nickel data (see Figs. 12c and 13c). In this q^2 region strong coherent production should dominate Coulomb production. For the uranium data, we derive in this q^2 region an upper limit of Σ^0 events at the 90% confidence level from a fit of the background distribution and the expected Σ^0 signal shape on top of it. This upper limit is obtained in each momentum bin separately and is quoted in Table 1. Having obtained this data we argue as follows:

i) Any Σ^0 signal due to either strong coherent or incoherent production has been taken into account already by the background subtraction, except for a possible interference with the Coulomb production. This is a consequence of the relatively small q^2 variation of the strong production mechanisms.

ii) Any strong coherent production amplitude interfering with Coulomb production vanishes at $q^2 = 0$ because the Λ-Σ^0 transition involves a spin flip just as the Coulomb production does. Therefore, we expect the differential strong coherent production cross-section to vary roughly like $q^2 \exp(-500\, q^2)$, where the slope parameter 500 $(GeV/c)^{-2}$ is a conservative estimate for the size of the uranium nucleus. Taking the worst case, we assume that the upper limit of strong Σ^0 production quoted above is solely due to interfering strong coherent production.

From the upper limit of strong coherent Σ^0 production in the region $0.002 < q^2 < 0.004$ $(GeV/c)^2$, we calculate the maximum strong coherent amplitude for $q^2 < 0.001$ $(GeV/c)^2$. The number of events due to pure Coulomb production is increased (decreased) by assuming maximum destructive (constructive) interference between the amplitudes of Coulomb and strong coherent production. The deviation from the event numbers without interference adds a systematic error to the Coulomb production cross-section on uranium.

The interference with strong coherent $\Delta I = 1$ production on nickel nuclei is expected to be suppressed by a factor $\{Z[(N-Z)/A]A^{2/3}\}_U / \{Z[(N-Z)/A]A^{2/3}\}_{Ni} \sim 41$ compared with uranium. Since our data do not show evidence for strong coherent production on uranium, we neglect any contribution of strong coherent production in the analysis of the nickel data.

4.3 The Σ^0 lifetime

Assuming that all Σ^0 events observed in the very forward direction are due to Coulomb production, we deduce from the measured cross-sections the Σ^0 lifetimes according to formula (3), taking into account the nuclear absorption correction. The lifetimes obtained at different momenta and for the two different target materials agree well with each other (Fig. 20). Averaging over the momentum bins, we get,

$$\tau_{\Sigma^0}^{(U)} = (0.69 \pm 0.13) \times 10^{-19} \text{ sec for uranium,}$$

and

$$\tau_{\Sigma^0}^{(Ni)} = (0.52 \pm 0.15) \times 10^{-19} \text{ sec for nickel,}$$

the two values being in agreement with each other. Combining both results we get

$$\tau_{\Sigma^0} = (0.62 \pm 0.10) \times 10^{-19} \text{ sec .}$$

However, taking into account the increased systematic errors due to possible strong coherent production in uranium, as quoted in Table 1, the weighted average of $\tau_{\Sigma^0}^{(U)}$ over all momentum bins changes to $(0.70 \pm 0.22) \times 10^{-19}$ sec. Combining uranium and nickel data again, we obtain the final result

$$\tau_{\Sigma^0} = (0.58 \pm 0.13) \times 10^{-19} \text{ sec ,}$$

where the quoted error includes a conservative estimate of the effect of a possible interference between the Coulomb and the strong coherent amplitudes.

5. COMPARISON WITH THEORETICAL PREDICTIONS

The Σ^0 lifetime is determined by the Σ^0-Λ magnetic transition moment $\mu_{\Sigma\Lambda}$ in Eq. (2). From our measurement of τ_{Σ^0} we get

$$|\mu_{\Sigma\Lambda}| = (1.90 \,^{+\ 0.26}_{-\ 0.19}) \frac{e\hbar}{2m_p c}$$

which agrees with the classical SU(3) prediction, Eq. (1). It should be noticed that a measurement of $\mu_{\Sigma\Lambda}$ provides a tool for the understanding of the SU(3) properties of the photon. The classical SU(3) predictions [1] for the magnetic moments of the members of the baryon octet and for the magnetic transition moment $\mu_{\Sigma\Lambda}$ are based on the assumption that the photon is well described by an SU(3) octet (ρ^0, ω and ϕ, with $\omega - \phi$ mixing), and has no SU(3) singlet contribution. However, theoretical models are discussed (e.g. charm schemes), which require in addition to the usual octet part a term in the electromagnetic current which transforms like an SU(3) singlet. This, in turn, leads to a revision of the classical SU(3) relations for the magnetic moments as pointed out by Gupta and Kögerler [14]. Their prediction,

$$\mu_{\Sigma\Lambda} = \sqrt{3}(\mu_\Lambda - \mu_n) = 2.15 \frac{e\hbar}{2m_p c} \ ,$$

incorporating an SU(3) singlet contribution of the photon, is also consistent with our result.

Acknowledgements

We should like to thank Dr. F. Vannucci for taking part in the early stage of the experiment. We are indebted to Prof. K. Gottfried for his estimate of the ρ^0-exchange contribution, and to Prof. C. Wilkin for his calculation of the form factor and the nuclear absorption correction. We are grateful for the on-line programming assistance of Dr. E.M. Rimmer and Mr. A. Lacourt. We thank Messrs. G. Laverrière, P. Ponting, P. Schilly and Dr. M. Vysočanský for their technical help.

REFERENCES

[1] S. Coleman and S.L. Glashow, Phys. Rev. Letters 6 (1961) 423.

[2] R. Van Royen and V.F. Weisskopf, Nuovo Cimento 50A (1967) 617.

[3] D.H. Davis, R. Levi Setti, M. Raymund and G. Tomasini, Phys. Rev. 127 (1962) 605.

[4] J. Dreitlein and H. Primakoff, Phys. Rev. 125 (1962) 1671.

[5] W.S.C. Williams, Nuovo Cimento 19 (1961) 1278.
I.Ya. Pomeranchuk and I.M. Shmushkevitch, Nuclear Phys. 23 (1961) 452.

[6] F. Dydak, C. Geweniger, F.L. Navarria, P. Steffen, J. Steinberger, F. Vannucci, H. Wahl, E.G.H. Williams, F. Eisele, K. Kleinknecht and V. Lüth, Nuclear Phys. B102 (1976) 253.

[7] A. Browman, J. De Wire, B. Gittelman, K.M. Hanson, D. Larson, E. Loh and R. Lewis, Phys. Rev. Letters 33 (1974) 1400.
A. Browman, J. De Wire, B. Gittelman, K.M. Hanson, E. Loh and R. Lewis, Phys. Rev. Letters 32 (1974) 1067.

[8] C. Wilkin, private communication.

[9] G. Fäldt, Nuclear Phys. B43 (1972) 591.

[10] J.H. Dieperink, P. Steffen, J. Steinberger, T. Trippe, F. Vannucci, H. Wahl, D. Zanello, H. Filthuth, K. Kleinknecht, V. Lüth, P. Mokry, H. Schneider, M. Vysočanský and G. Zech, Proc. Internat. Conf. on Instrumentation for High-Energy Physics, Dubna, 1970 (JINR, Dubna, 1971), p. 251.
P. Schilly, P. Steffen, J. Steinberger, T. Trippe, F. Vannucci, H. Wahl, K. Kleinknecht and V. Lüth, Nuclear Instrum. Methods 91 (1971) 221.
V. Lüth, CERN NP Internal Report 74-7 (1974), and thesis, Universität Heidelberg, 1974.
F. Vannucci, thesis, Université Paris-Sud, 1973.

[11] H. Messel and D.F. Crawford, Electron-photon shower distribution function (Pergamon Press, Oxford, 1970).

[12] F. Dydak, G. Laverrière, F.L. Navarria, P. Steffen, P. Schilly, E.G.H. Williams, H. Taureg and M. Vysočanský, Performance of a lead-glass detector for high-energy gamma rays, to be published in Nuclear Instrum. Methods.
H. Taureg, CERN EP Internal Report 76-6 (1976), and thesis, Universität Heidelberg, 1976.

[13] K. Gottfried, private communication.

[14] V. Gupta and R. Kögerler, Phys. Letters 56B (1975) 473.

Table 1

Σ^0 production

on uranium

p_{Σ^0} (GeV/c)	Number of Σ^0 events	σ_{meas} (mb)	σ_{theor} a) (mb)	τ_{Σ^0} (10^{-19} sec)	Upper limit c) for strong coherent production	τ_{Σ^0} d) (10^{-19} sec)
9-11	66 ± 26	3.6 ± 1.5	2.11 (3.06)	0.59 ± 0.25	29	0.59 ± 0.44
11-13	73 ± 27	2.8 ± 1.1	2.52 (3.52)	0.90 ± 0.35	32	0.90 ± 0.63
13-15	51 ± 25	2.5 ± 1.3	2.89 (3.92)	1.16 ± 0.60	24	1.16 ± 0.89
15-17	60 ± 16	5.2 ± 1.5	3.21 (4.28)	0.62 ± 0.18	15	0.62 ± 0.31
17-19	18 ± 11	4.3 ± 2.8	3.51 (4.59)	0.82 ± 0.53	8	0.82 ± 0.68
				0.69 ± 0.13 b)		0.70 ± 0.22 b)

on nickel

p_{Σ^0} (GeV/c)	Number of Σ^0 events	σ_{meas} (mb)	σ_{theor} a) (mb)	τ_{Σ^0} (10^{-19} sec)
11-13	33 ± 14	0.58 ± 0.26	0.280 (0.326)	0.48 ± 0.22
13-15	26 ± 15	0.49 ± 0.30	0.316 (0.363)	0.64 ± 0.39
15-17	23 ± 11	0.68 ± 0.34	0.348 (0.396)	0.51 ± 0.26
17-19	7 ± 7	0.56 ± 0.59	0.376 (0.425)	0.67 ± 0.71
				0.52 ± 0.15 b)

a) The theoretical cross-section is quoted for $\tau_{\Sigma^0} = 1.0 \times 10^{-19}$ sec. For comparison, the theoretical cross-sections without the absorption correction are given in brackets.

b) Weighted average.

c) Upper limit for strong coherent Σ^0 production in the region $0.002 < q^2 < 0.004$ $(GeV/c)^2$.

d) The error includes a possible interference with strong coherent Σ^0 production.

Figure captions

Fig. 1 : Primakoff production of Σ^0 hyperons on nuclei.

Fig. 2 : Plan view and elevation of the apparatus.

Fig. 3 : Invariant mass $m(p,\pi^-)$ distribution of accepted Λ-monitor events.

Fig. 4 : R_Λ^2 distribution of accepted Λ-monitor events (R_Λ^2 is the squared distance of the Λ trajectory from the proton target centre).

Fig. 5 : Momentum p_Λ distribution of accepted Λ-monitor events.

Fig. 6 : Λ acceptance as a function of the Λ momentum.

Fig. 7 : Σ^0 acceptance as a function of the $\Lambda + \gamma$ momentum.

Fig. 8 : Photon energy distribution of accepted $\Sigma^0 \to \Lambda + \gamma$ Monte Carlo events, in the laboratory system. The dashed line shows the efficiency of the "dynode bit" setting of the apparatus as a function of the photon energy.

Fig. 9 : The histograms show the experimental q^2 resolution of Σ^0 Monte Carlo events. For comparison, the curves indicate the q^2 dependence of the Coulomb production cross-section.

Fig. 10 : Invariant mass $m(p,\pi^-)$ distribution of $(\Lambda + \gamma)$ events.

Fig. 11 : Invariant mass $m(\Lambda,\gamma)$ distribution of all $(\Lambda + \gamma)$ events.

Fig. 12 : Invariant mass $m(\Lambda,\gamma)$ distribution for $(\Lambda + \gamma)$ momenta between 13 and 19 GeV/c, (a) for $q^2 < 0.001$ $(GeV/c)^2$, (b) for $0.001 < q^2 < 0.002$ $(GeV/c)^2$, and (c) for $0.002 < q^2 < 0.004$ $(GeV/c)^2$, for uranium data. In (a) the dashed histogram shows the mass resolution for Σ^0 Monte Carlo events.

Fig. 13 : Invariant mass $m(\Lambda,\gamma)$ distribution for $(\Lambda + \gamma)$ momenta between 13 and 19 GeV/c, (a) for $q^2 < 0.001$ $(GeV/c)^2$, (b) for $0.001 < q^2 < 0.002$ $(GeV/c)^2$, and (c) for $0.002 < q^2 < 0.004$ $(GeV/c)^2$, for nickel data. In (a) the dashed histogram shows the mass resolution for Σ^0 Monte Carlo events.

Fig. 14 : q^2 distribution of uranium data for different mass $m(\Lambda,\gamma)$ bins with a width of 30 MeV/c^2, ranging from 1.115 to 1.265 GeV/c^2. The curve indicates the background fit in the Σ^0 mass bin. The shaded area above the background curve denotes the Coulomb production signal.

Fig. 15 : q^2 distribution of nickel data for different mass $m(\Lambda,\gamma)$ bins with a width of 30 MeV/c^2, ranging from 1.115 to 1.265 GeV/c^2. The curve indicates the background fit in the Σ^0 mass bin. The shaded area above the background curve denotes the Coulomb production signal.

Fig. 16 : q^2 distribution of Monte Carlo generated background events for different mass $m(\Lambda,\gamma)$ bins with a width of 30 MeV/c^2, ranging from 1.115 to 1.265 GeV/c^2. The events are due to $\Xi^0 \rightarrow \Lambda\pi^0$ decays, with one undetected photon from the $\pi^0 \rightarrow 2\gamma$ decay.

Fig. 17 : q^2 distribution of uranium data, for masses in the Σ^0 bin $1.175 < m(\Lambda,\gamma) < 1.205$ GeV/c^2, and $(\Lambda + \gamma)$ momenta between 13 and 19 GeV/c^2. The dashed line represents the expected q^2 resolution of Primakoff events. The curve indicates the background fit.

Fig. 18 : q^2 distribution of nickel data, for masses in the Σ^0 bin $1.175 < m(\Lambda,\gamma) < 1.205$ GeV/c^2, and $(\Lambda + \gamma)$ momenta between 13 and 19 GeV/c^2. The dashed line represents the expected q^2 resolution of Primakoff events. The curve indicates the background fit.

Fig. 19 : Total cross-section of the Primakoff production σ_{Σ^0}, as a function of the $(\Lambda + \gamma)$ momentum, (a) for uranium data and (b) for nickel data. The full line represents the theoretical Primakoff cross-section for $\tau_{\Sigma^0} = 0.69 \times 10^{-19}$ sec (Fig. 19a) and $\tau = 0.52 \times \times 10^{-19}$ sec (Fig. 19b), respectively.

Fig. 20 : τ_{Σ^0}, as a function of the $(\Lambda + \gamma)$ momentum, both for uranium and nickel data.

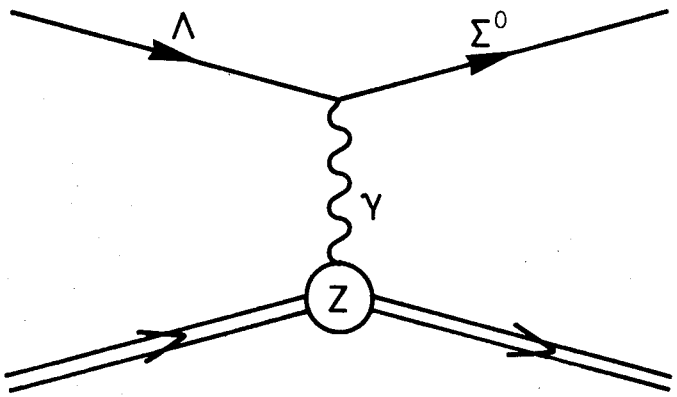

Fig. 1

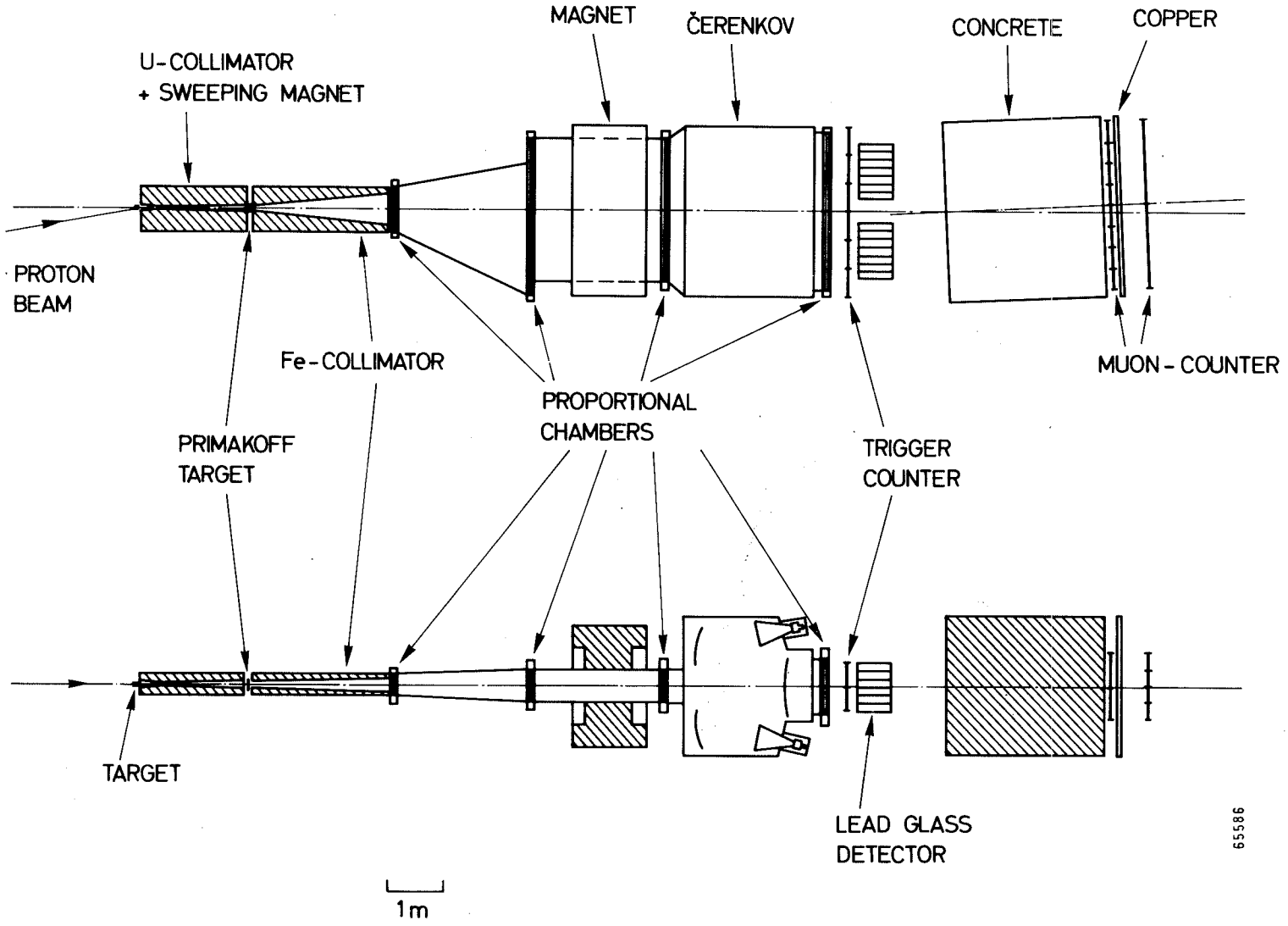
MAGNET
ČERENKOV
CONCRETE
COPPER
U-COLLIMATOR
+ SWEEPING MAGNET
PROTON
BEAM
Fe-COLLIMATOR
PROPORTIONAL
CHAMBERS
MUON-COUNTER
PRIMAKOFF
TARGET
TRIGGER
COUNTER
TARGET
LEAD GLASS
DETECTOR
1m
65586

Fig. 2

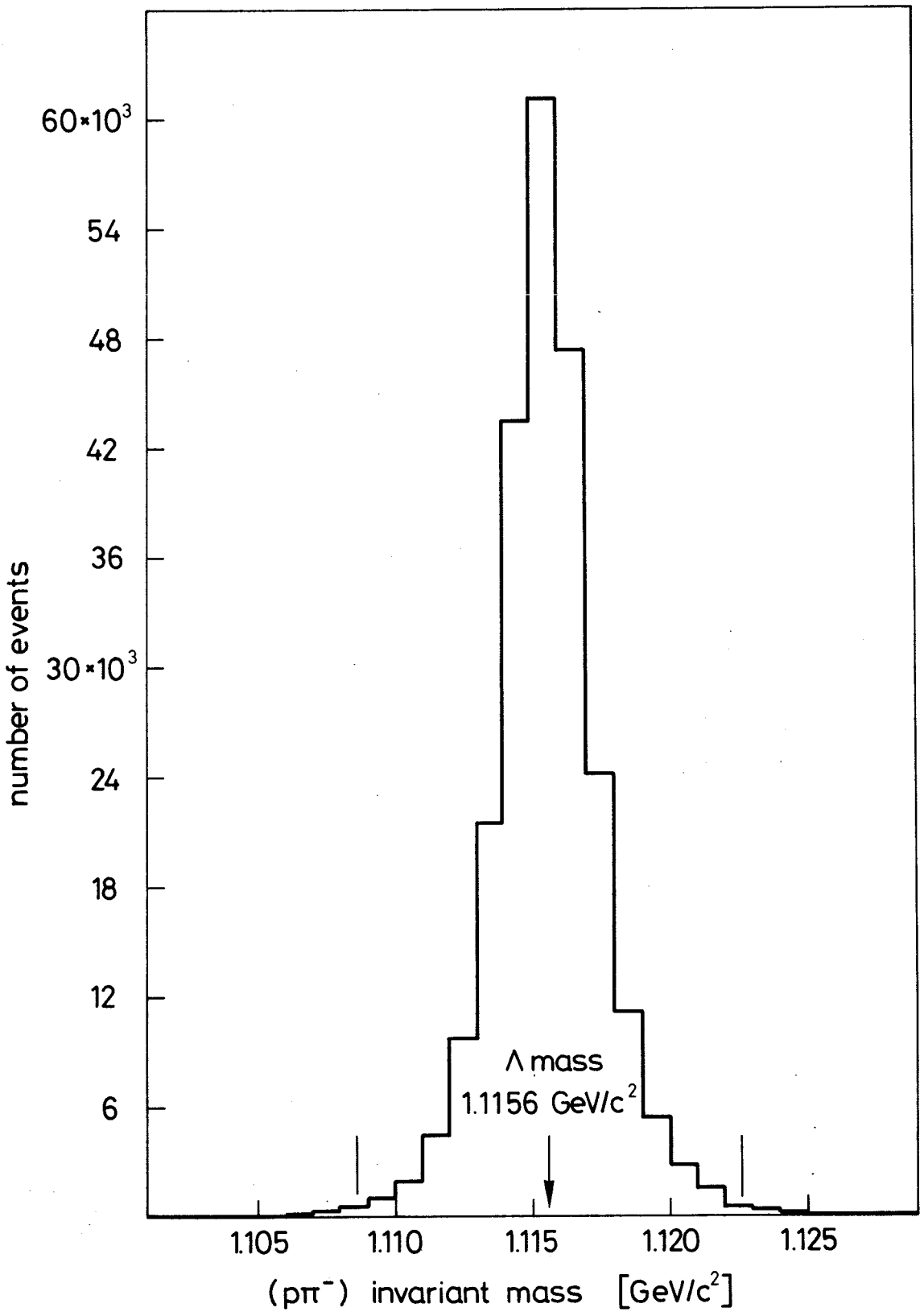
60×10³
54
48
42
36
30×10³
24
18
12
6
number of events
Λ mass
1.1156 GeV/c²
1.105
1.110
1.115
1.120
1.125
(pπ⁻) invariant mass [GeV/c²]

Fig. 3

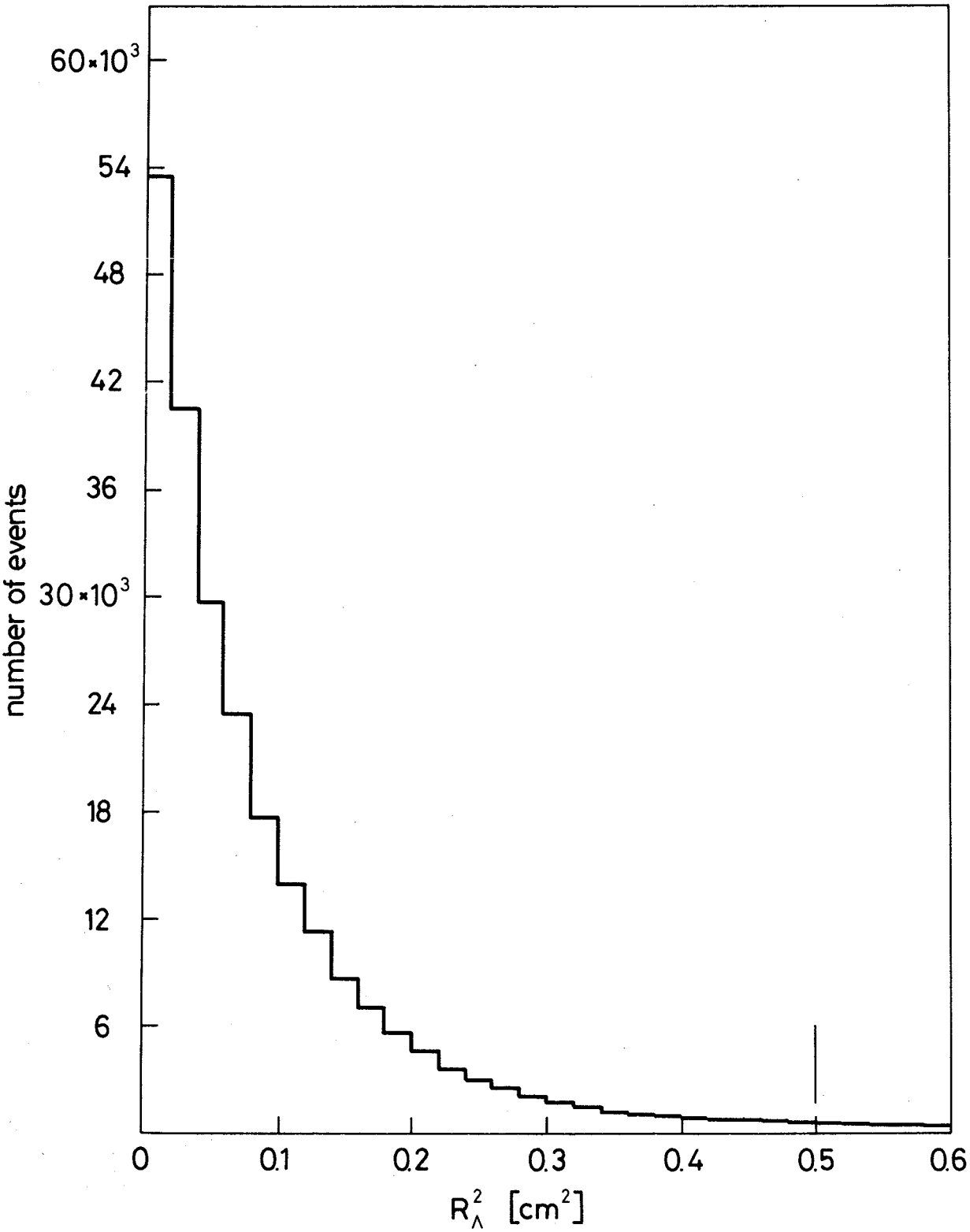
60×10³
54
48
42
36
30×10³
24
18
12
6
number of events
0
0.1
0.2
0.3
0.4
0.5
0.6
R²Λ [cm²]

Fig. 4

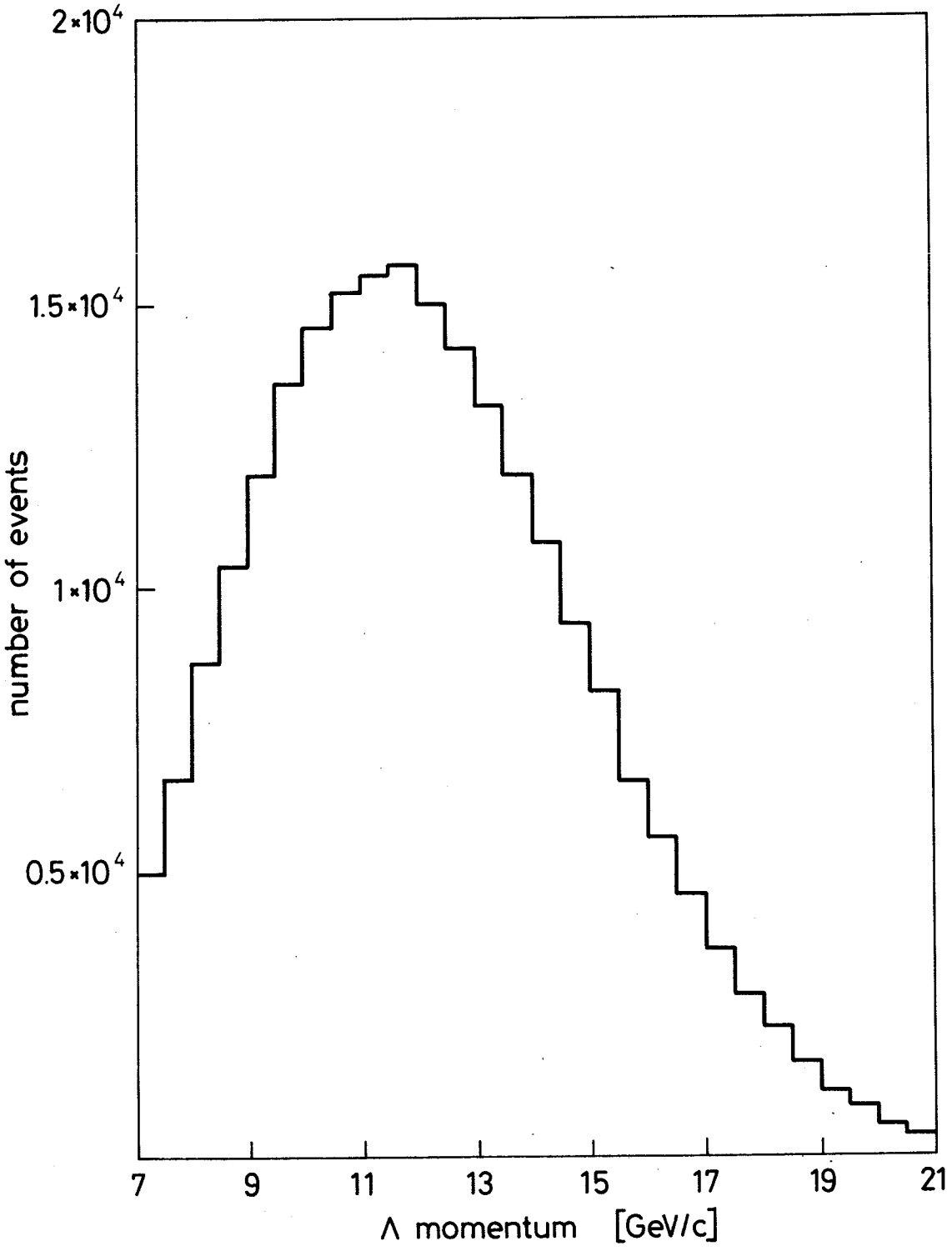
2×10⁴
1.5×10⁴
1×10⁴
0.5×10⁴
number of events
7
9
11
13
15
17
19
21
Λ momentum [GeV/c]

Fig. 5

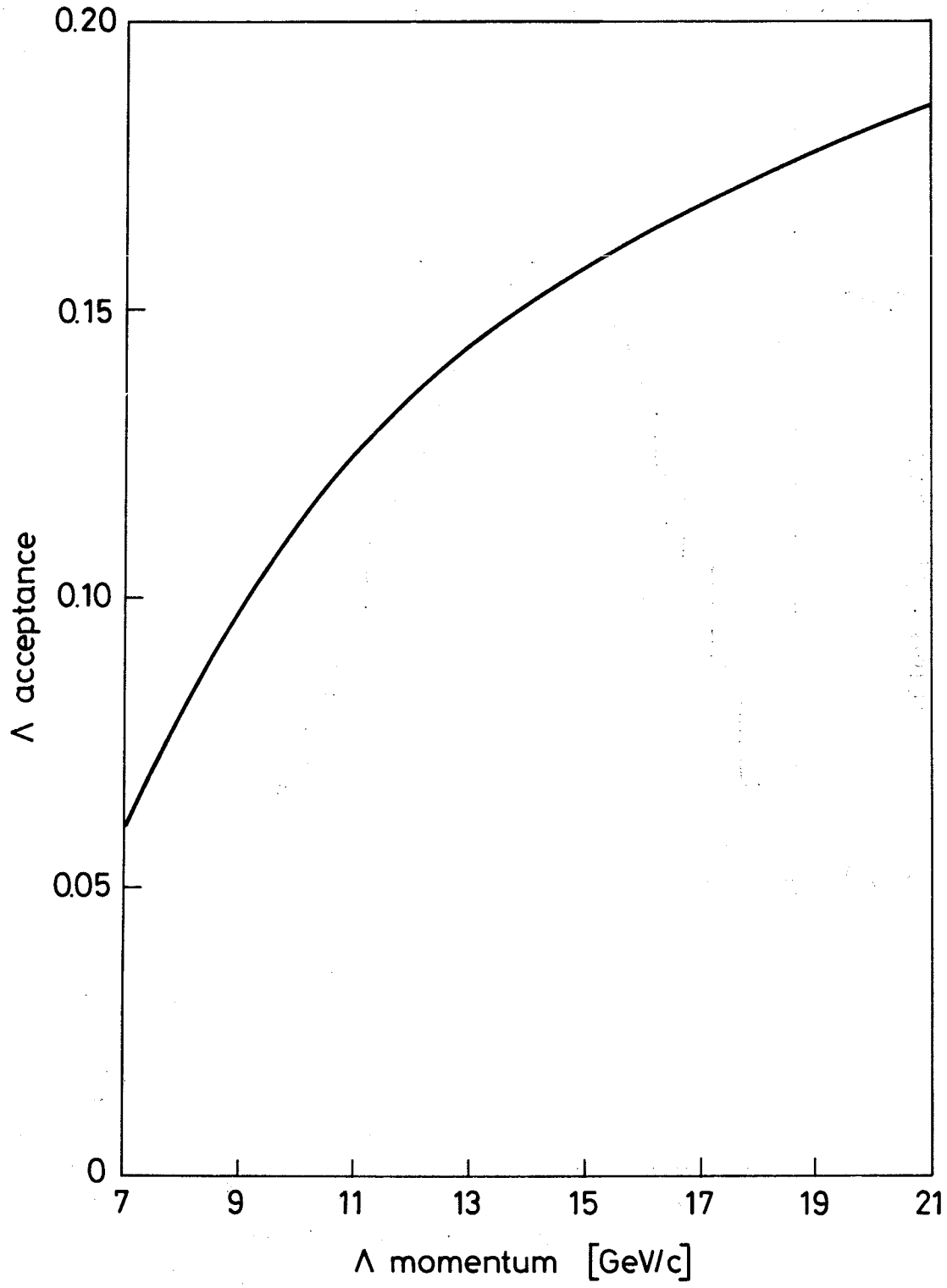
0.20
0.15
0.10
0.05
0
Λ acceptance
7
9
11
13
15
17
19
21
Λ momentum [GeV/c]

Fig. 6

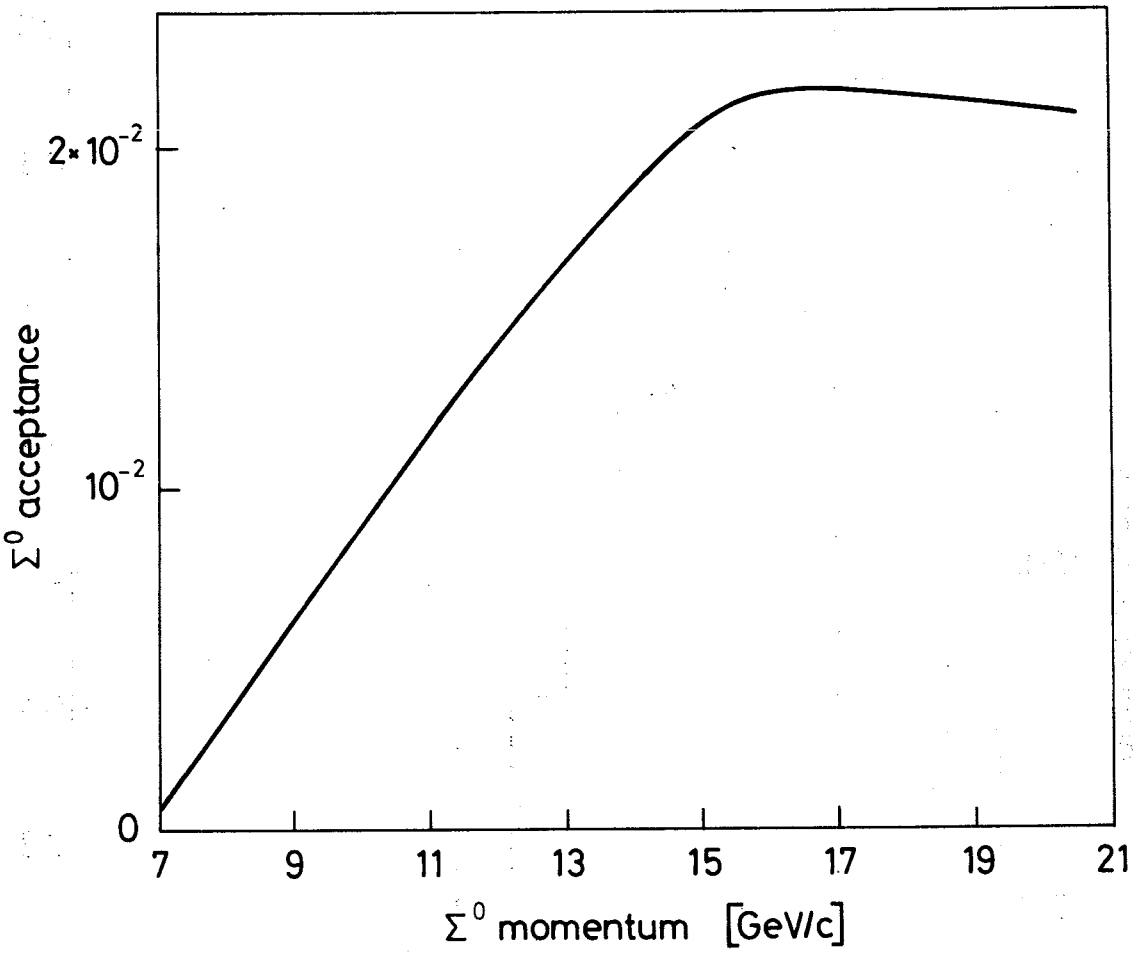

Fig. 7

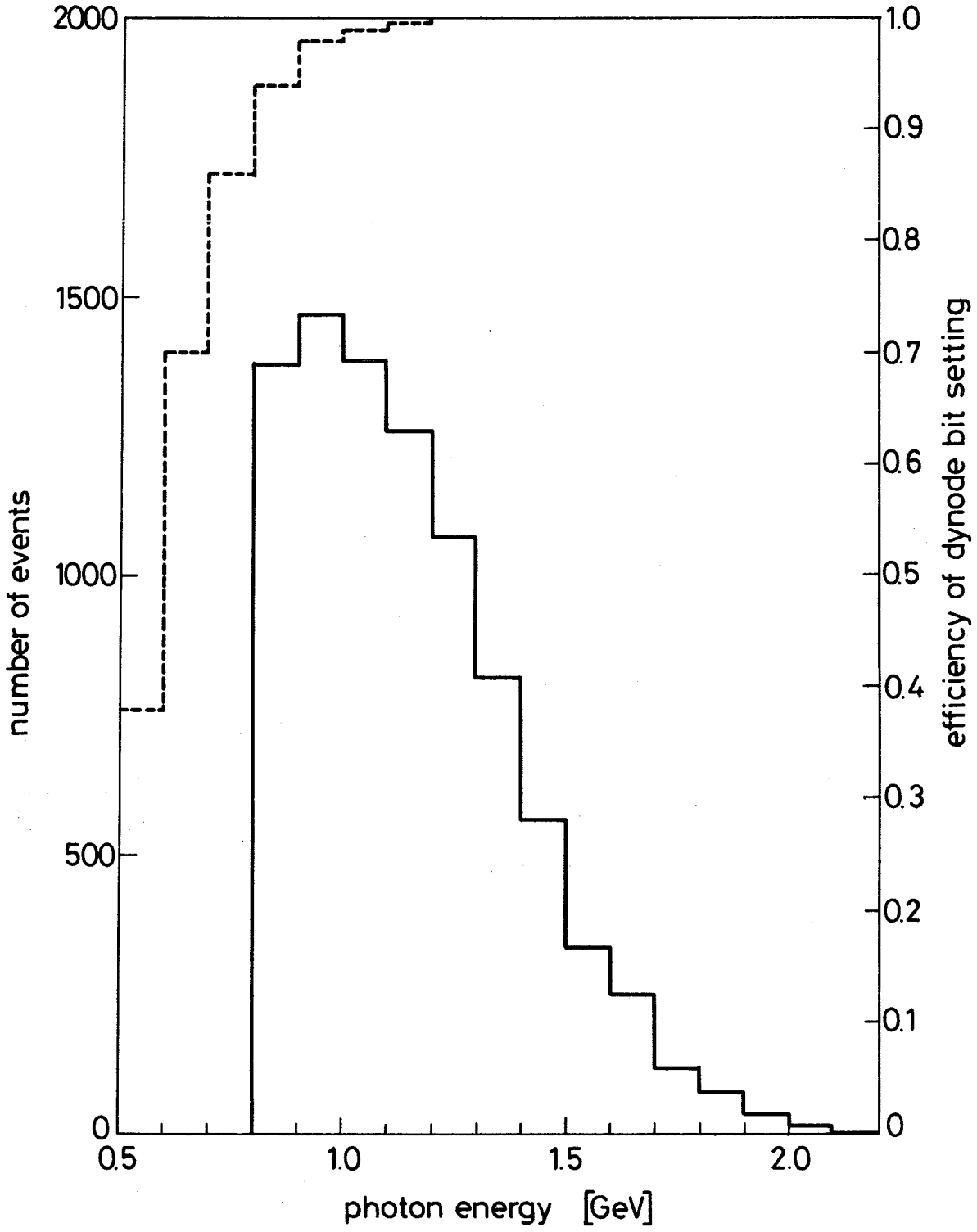
2000
1500
1000
500
0
number of events
1.0
0.9
0.8
0.7
0.6
0.5
0.4
0.3
0.2
0.1
0
efficiency of dynode bit setting
0.5
1.0
1.5
2.0
photon energy [GeV]

Fig. 8

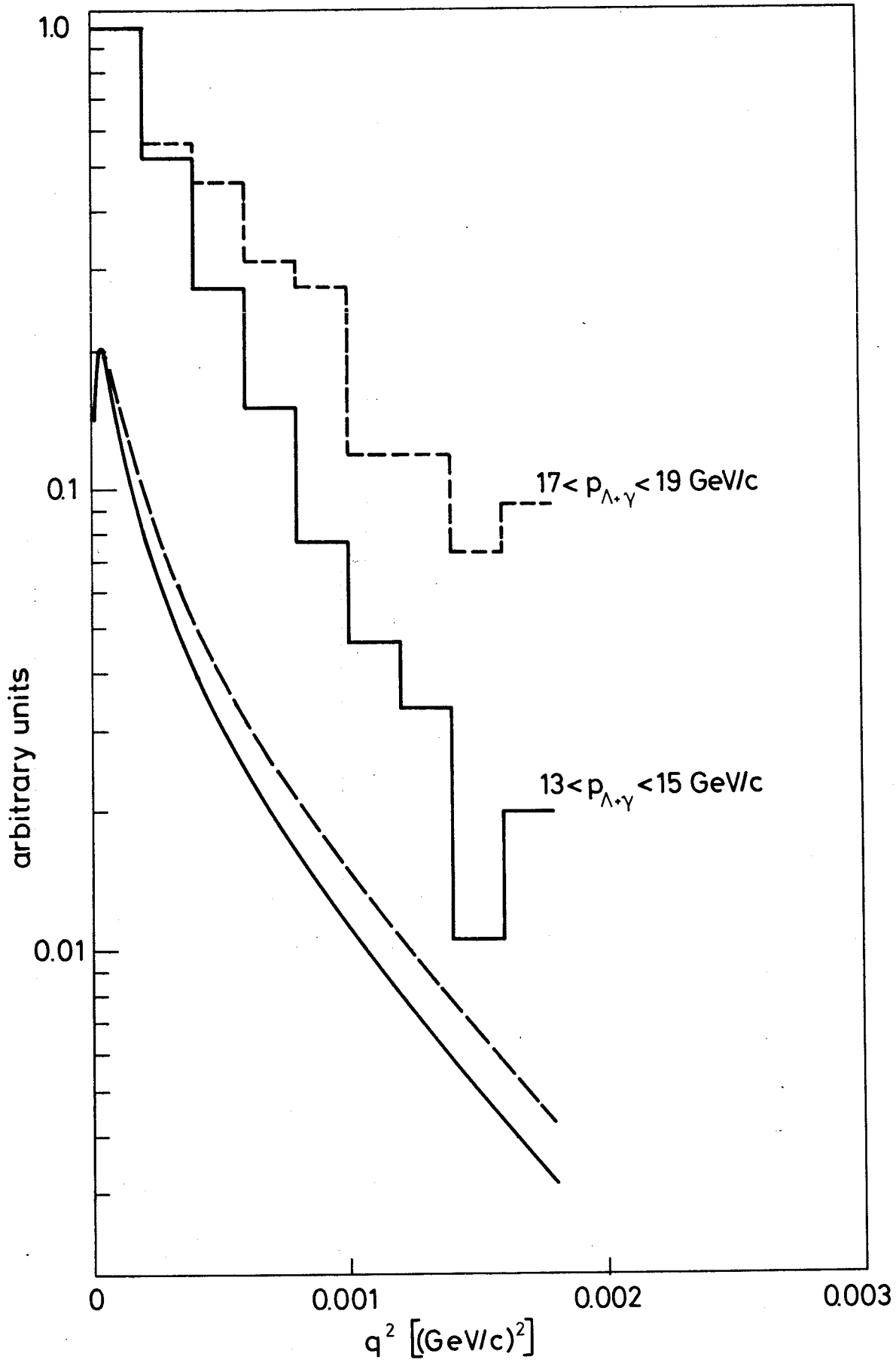
1.0
0.1
0.01
arbitrary units
17< p_{Λ*γ} <19 GeV/c
13< p_{Λ*γ} <15 GeV/c
0
0.001
0.002
0.003
q² [(GeV/c)²]

Fig. 9

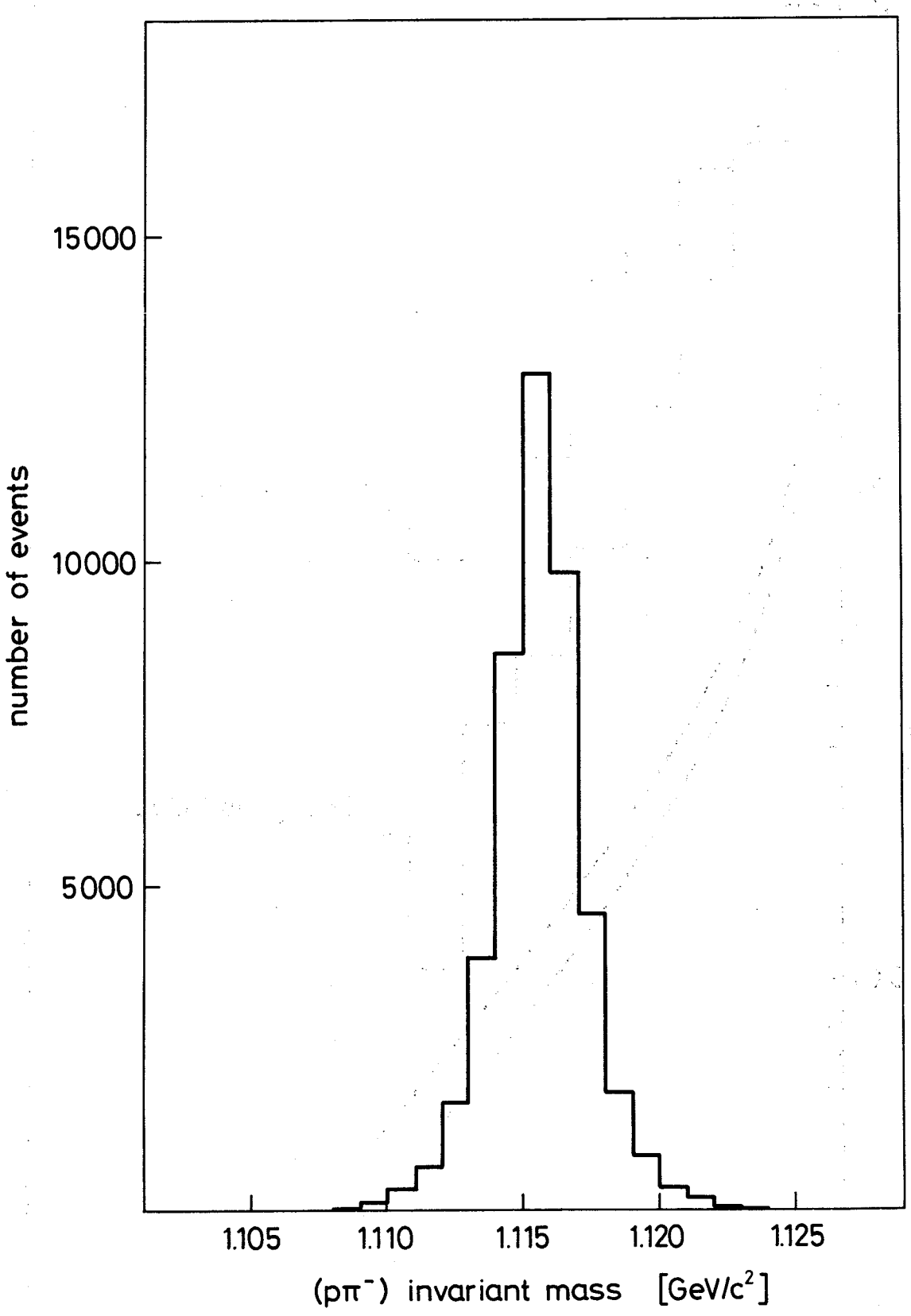
15000
10000
5000
number of events
1.105
1.110
1.115
1.120
1.125
(pπ⁻) invariant mass [GeV/c²]

Fig. 10

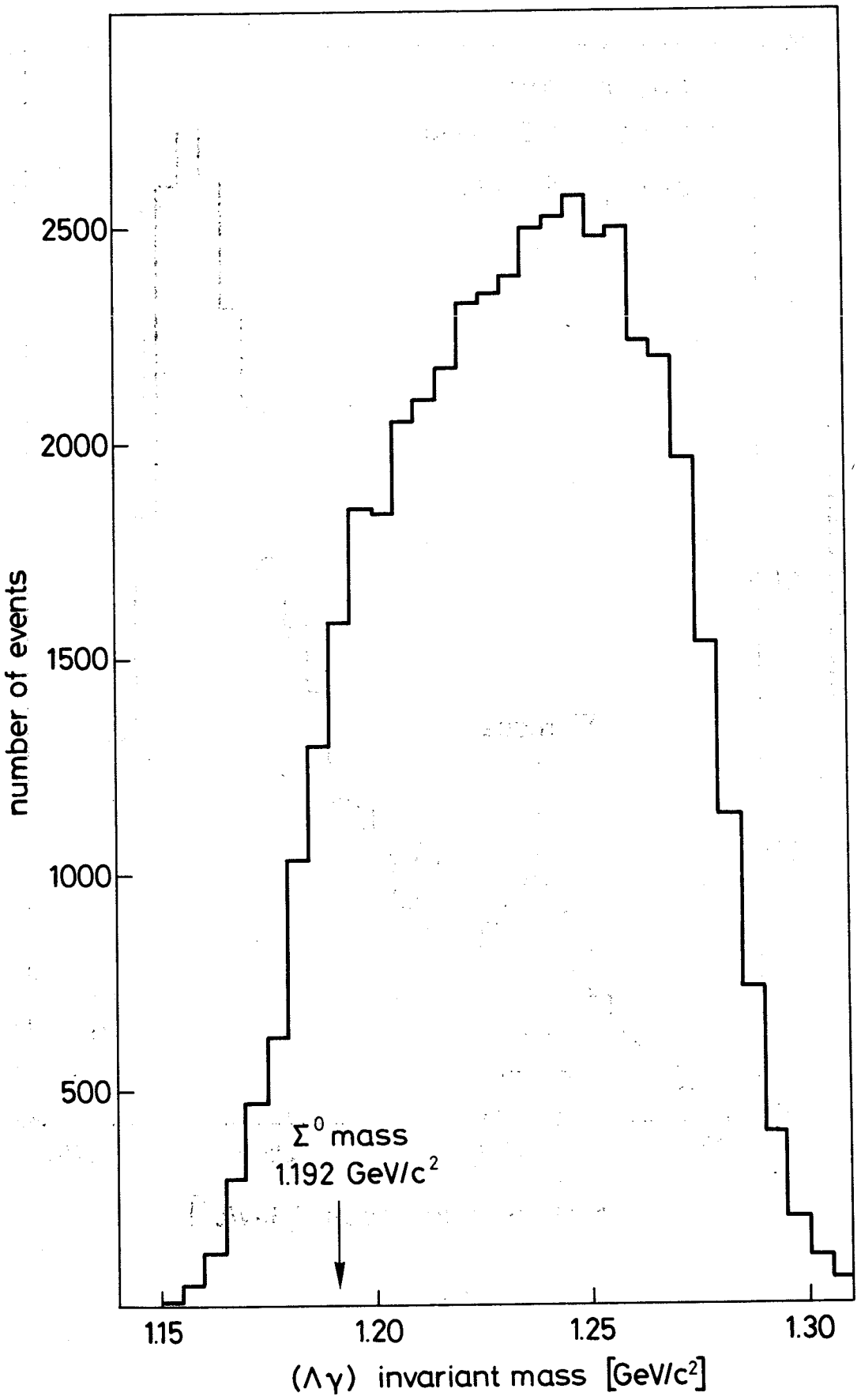
2500
2000
1500
1000
500
number of events
Σ⁰ mass
1.192 GeV/c²
1.15
1.20
1.25
1.30
(Λγ) invariant mass [GeV/c²]

Fig. 11

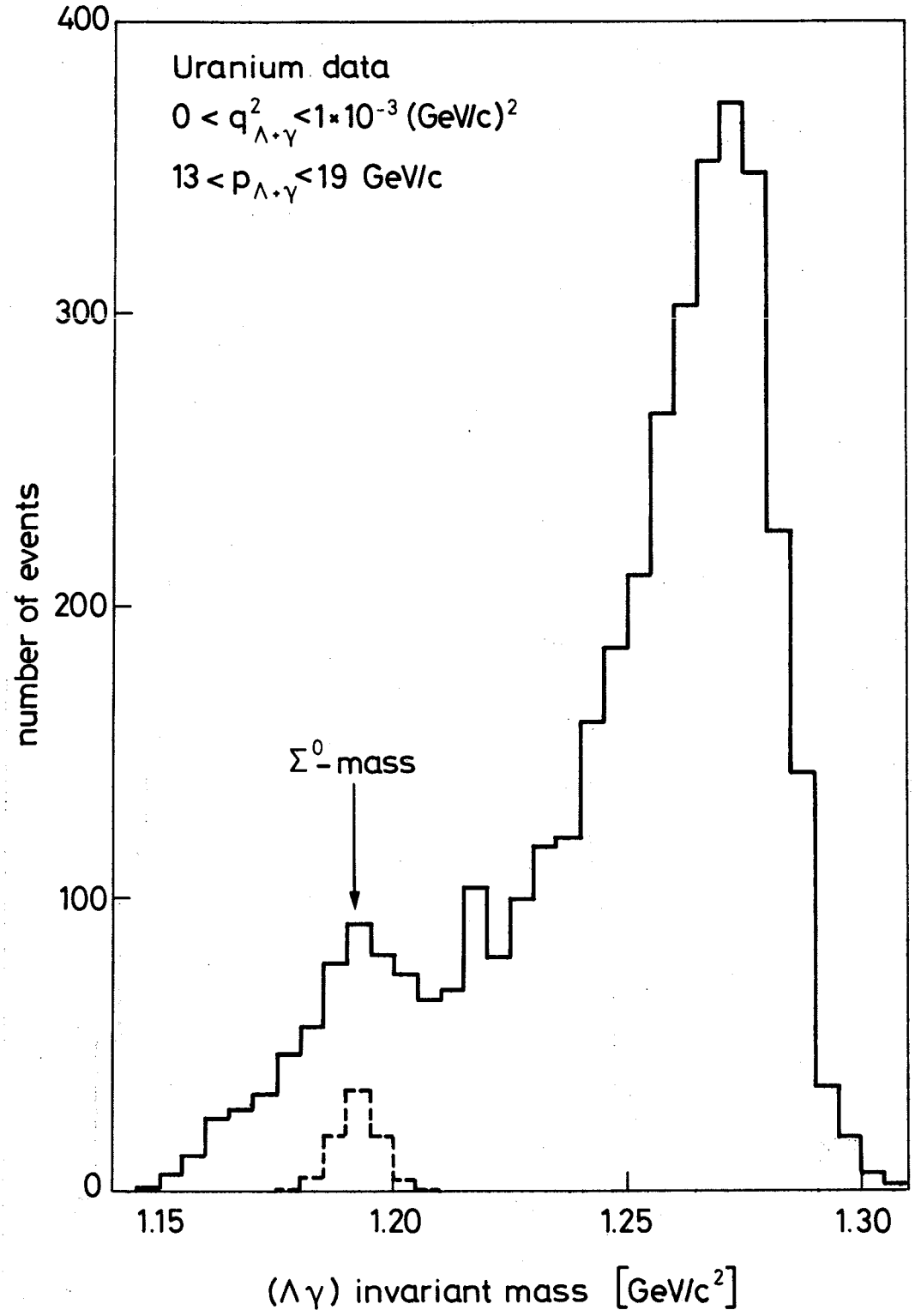
Uranium data
$0 < q^2_{\Lambda\cdot\gamma} < 1\cdot10^{-3}$ (GeV/c)^2
$13 < p_{\Lambda\cdot\gamma} < 19$ GeV/c
Σ^0-mass
number of events
400
300
200
100
0
1.15
1.20
1.25
1.30
$(\Lambda\gamma)$ invariant mass [GeV/c^2]

Fig. 12a

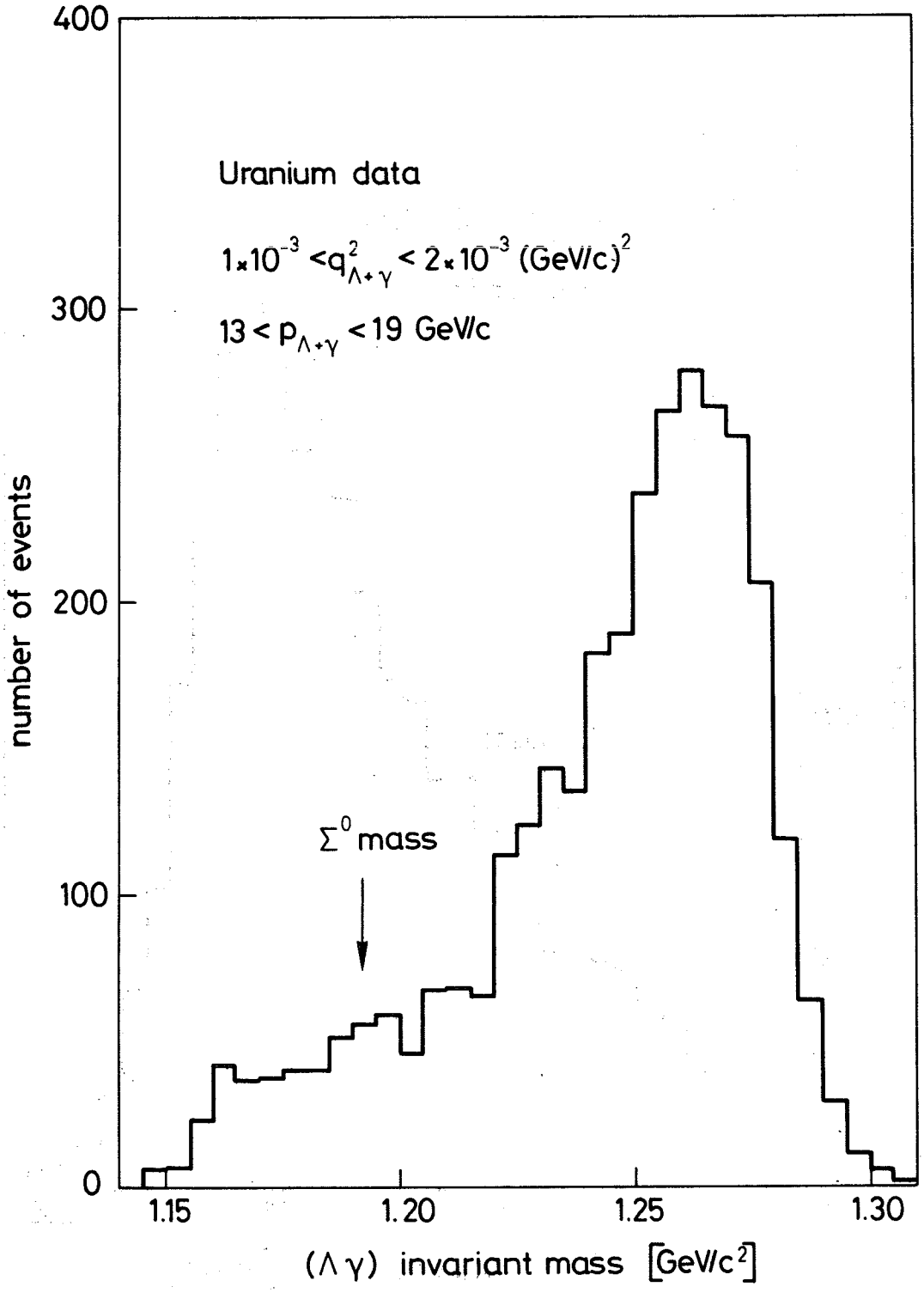
400
300
200
100
0
Uranium data
$1 \times 10^{-3} < q^2_{\Lambda+\gamma} < 2 \times 10^{-3}$ (GeV/c)^2
$13 < p_{\Lambda+\gamma} < 19$ GeV/c
number of events
Σ^0 mass
1.15
1.20
1.25
1.30
$(\Lambda\gamma)$ invariant mass [GeV/c^2]

Fig. 12b

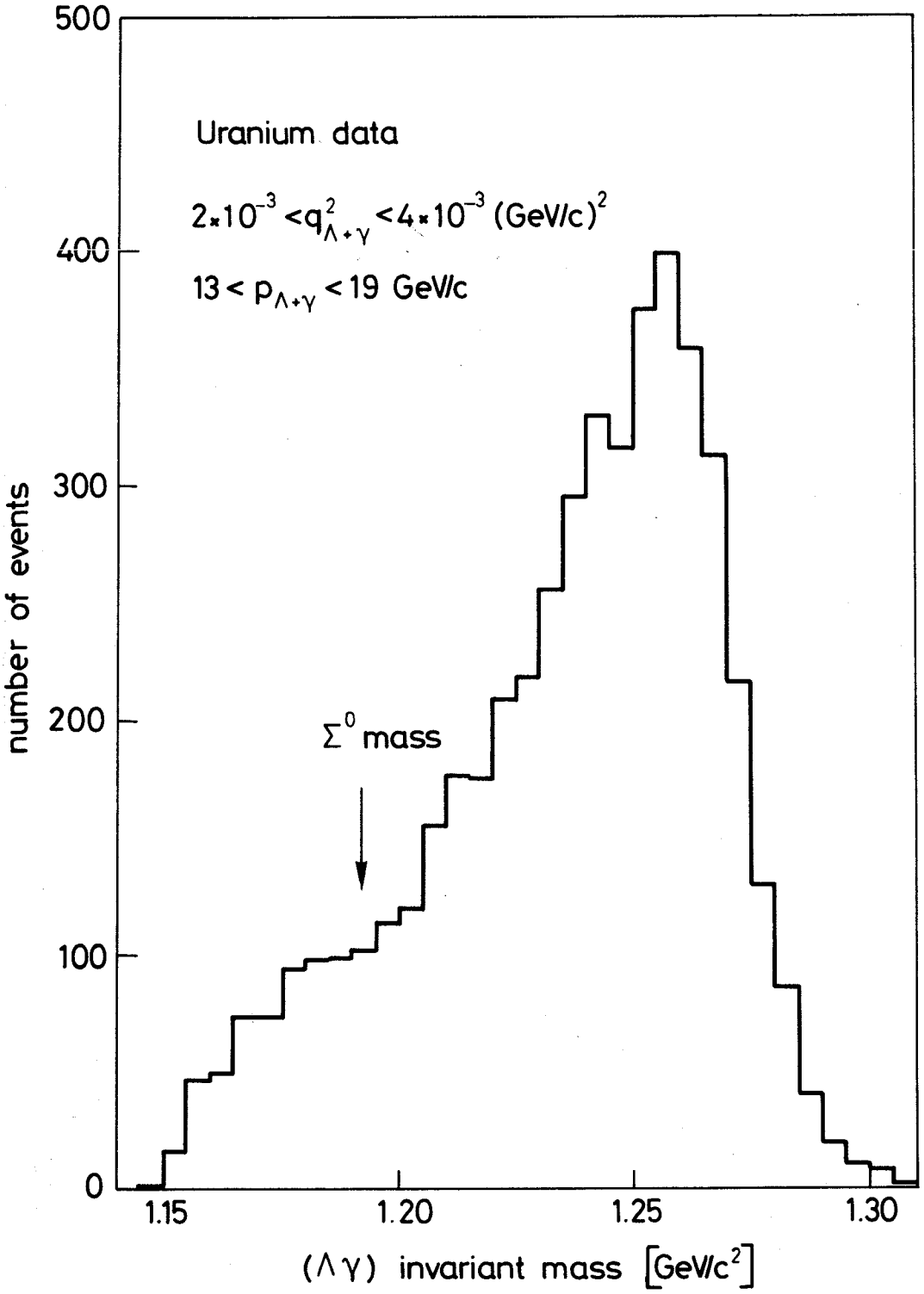
Uranium data
$2*10^{-3} < q^2_{\Lambda+\gamma} < 4*10^{-3}$ (GeV/c)^2
$13 < p_{\Lambda+\gamma} < 19$ GeV/c
Σ^0 mass
number of events
0
100
200
300
400
500
1.15
1.20
1.25
1.30
$(\Lambda\gamma)$ invariant mass [GeV/c^2]

Fig. 12c

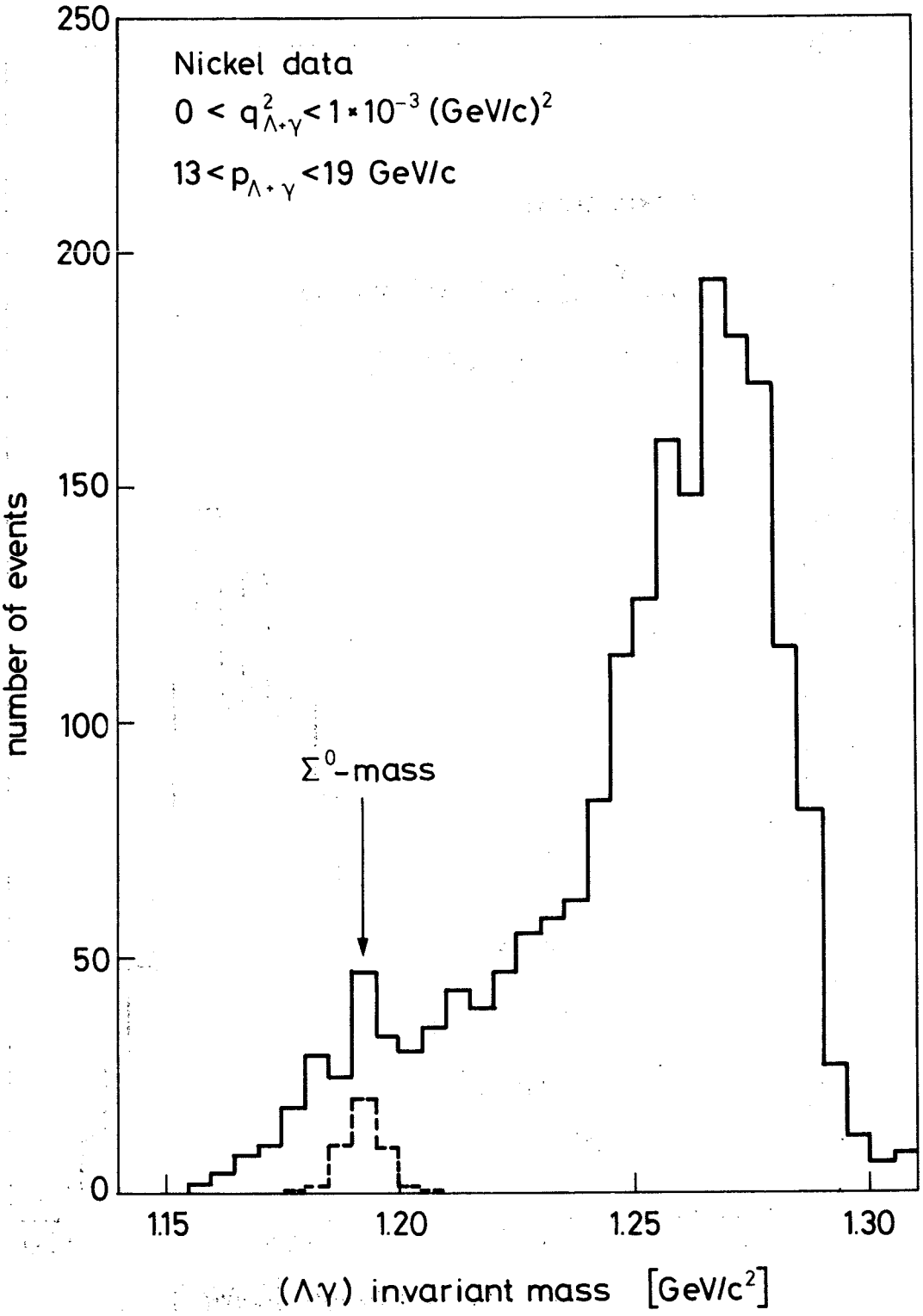
Nickel data
$0 < q^2_{\Lambda+\gamma} < 1 \times 10^{-3}$ (GeV/c)^2
$13 < p_{\Lambda+\gamma} < 19$ GeV/c
Σ^0-mass
number of events
250
200
150
100
50
0
1.15
1.20
1.25
1.30
$(\Lambda\gamma)$ invariant mass [GeV/c^2]

Fig. 13a.

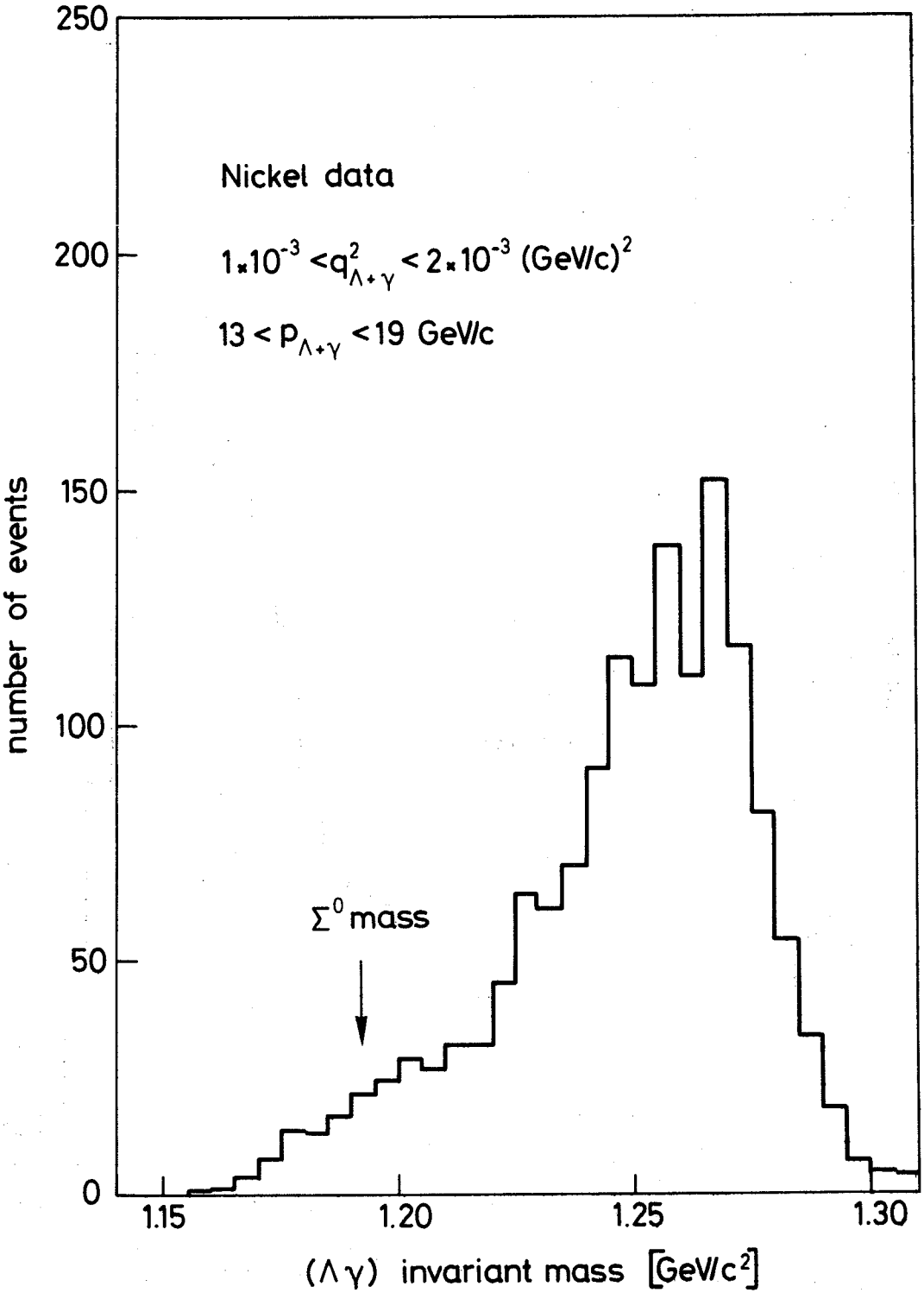
Nickel data
$1 \times 10^{-3} < q^2_{\Lambda+\gamma} < 2 \times 10^{-3}$ (GeV/c)^2
$13 < p_{\Lambda+\gamma} < 19$ GeV/c
Σ^0 mass
number of events
250
200
150
100
50
0
1.15
1.20
1.25
1.30
$(\Lambda\gamma)$ invariant mass [GeV/c^2]

Fig. 13b

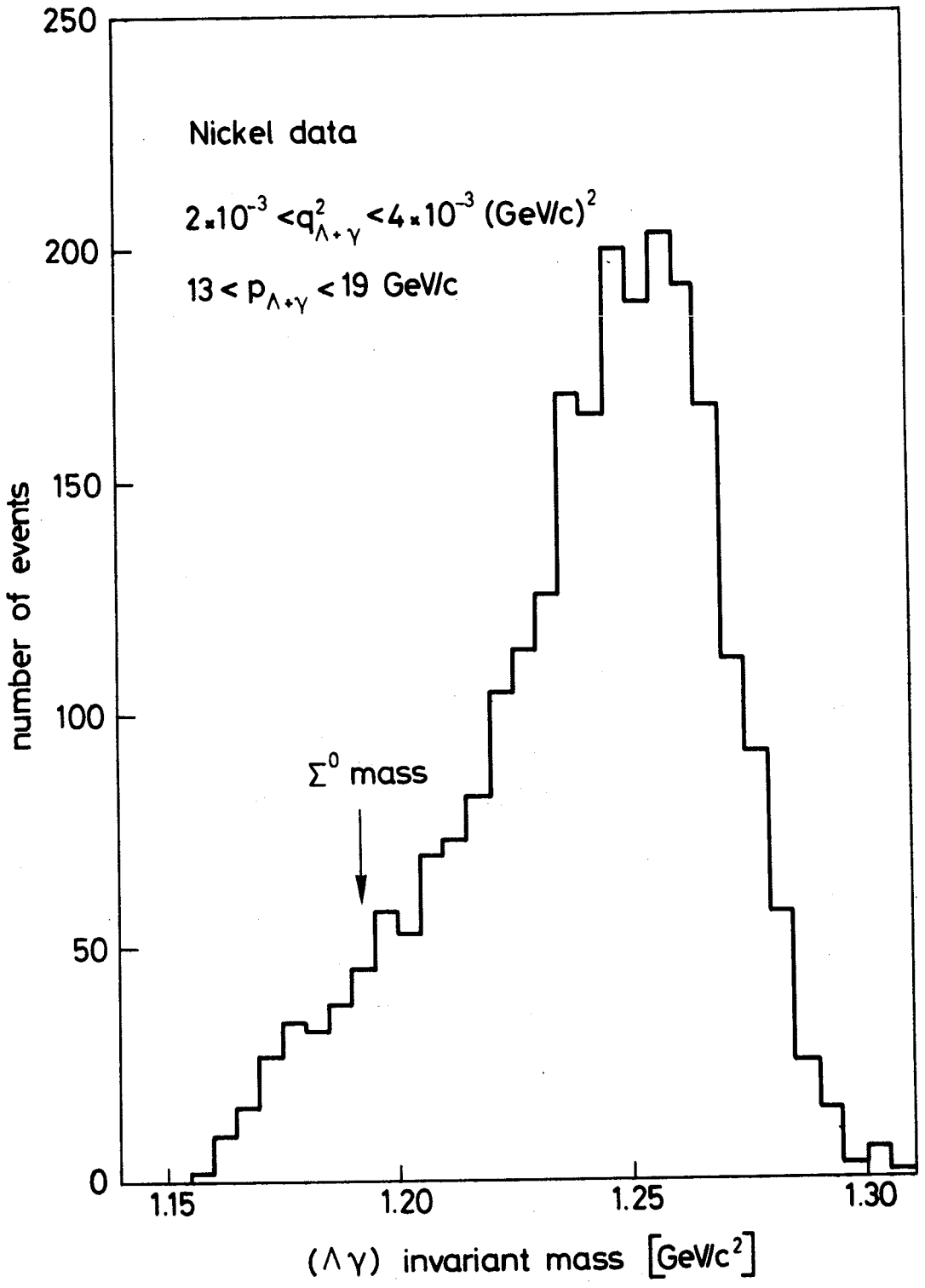
Nickel data
$2 \times 10^{-3} < q^2_{\Lambda+\gamma} < 4 \times 10^{-3}$ (GeV/c)^2
$13 < p_{\Lambda+\gamma} < 19$ GeV/c
Σ^0 mass
number of events
250
200
150
100
50
0
1.15
1.20
1.25
1.30
$(\Lambda\gamma)$ invariant mass [GeV/c^2]

Fig. 13c

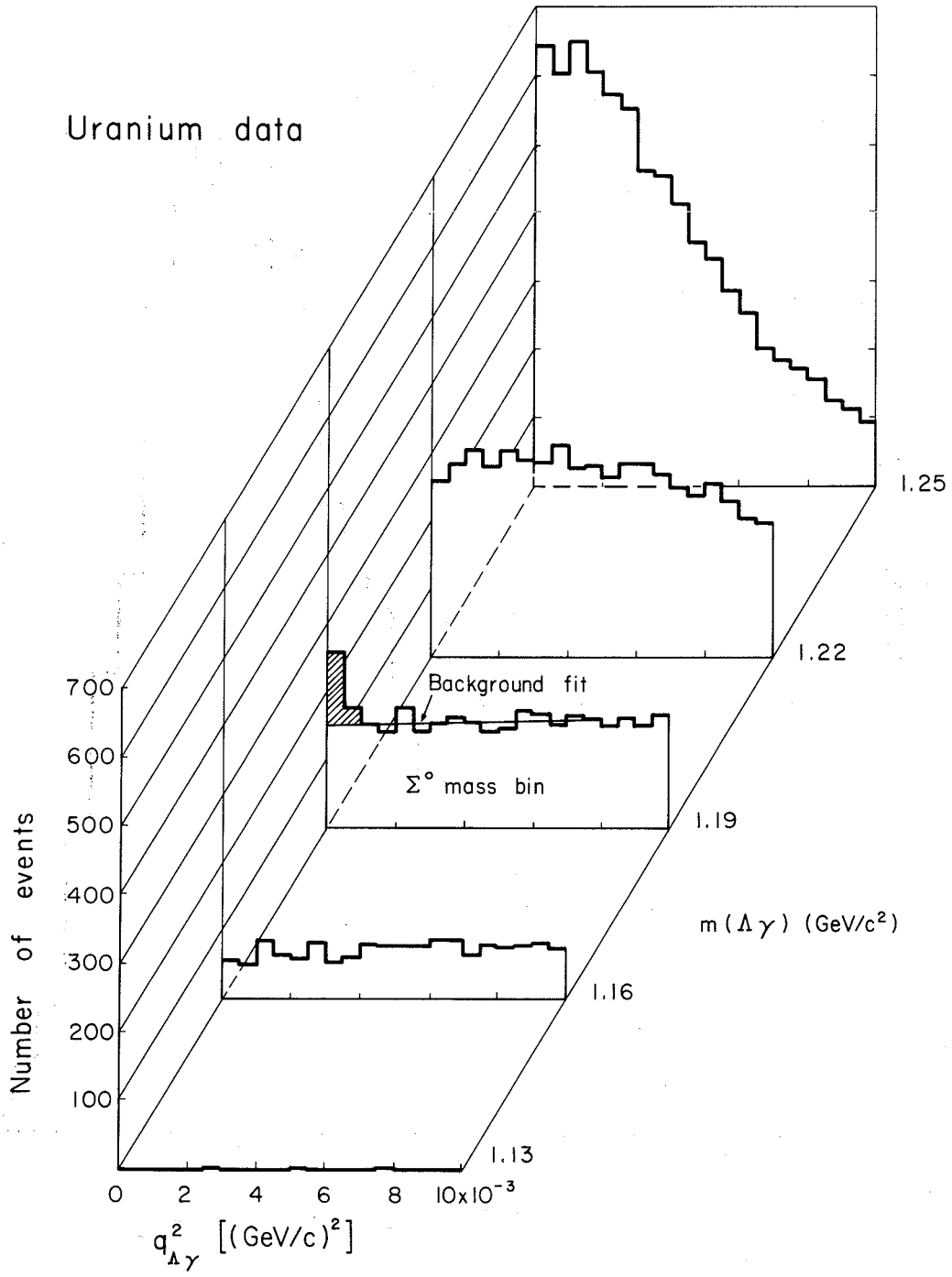
Uranium data
Number of events
700
600
500
400
300
200
100
Background fit
Σ° mass bin
1.25
1.22
1.19
1.16
1.13
m(Λγ) (GeV/c²)
0
2
4
6
8
10x10⁻³
q²Λγ [(GeV/c)²]

Fig. 14

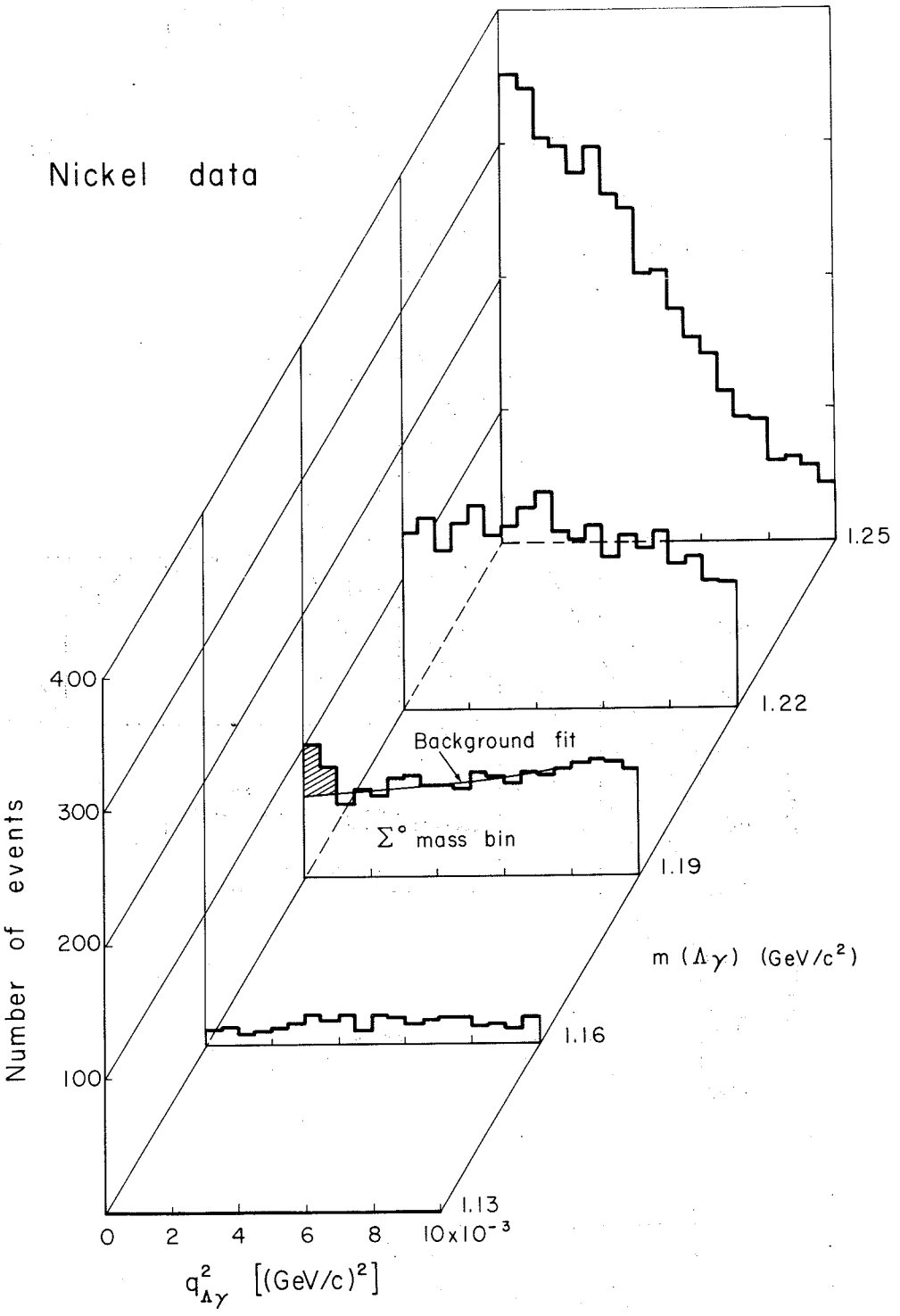
Nickel data
Number of events
400
300
200
100
Background fit
Σ° mass bin
1.25
1.22
1.19
1.16
1.13
m (Λγ) (GeV/c²)
0
2
4
6
8
10x10⁻³
q²Λγ [(GeV/c)²]

Fig. 15

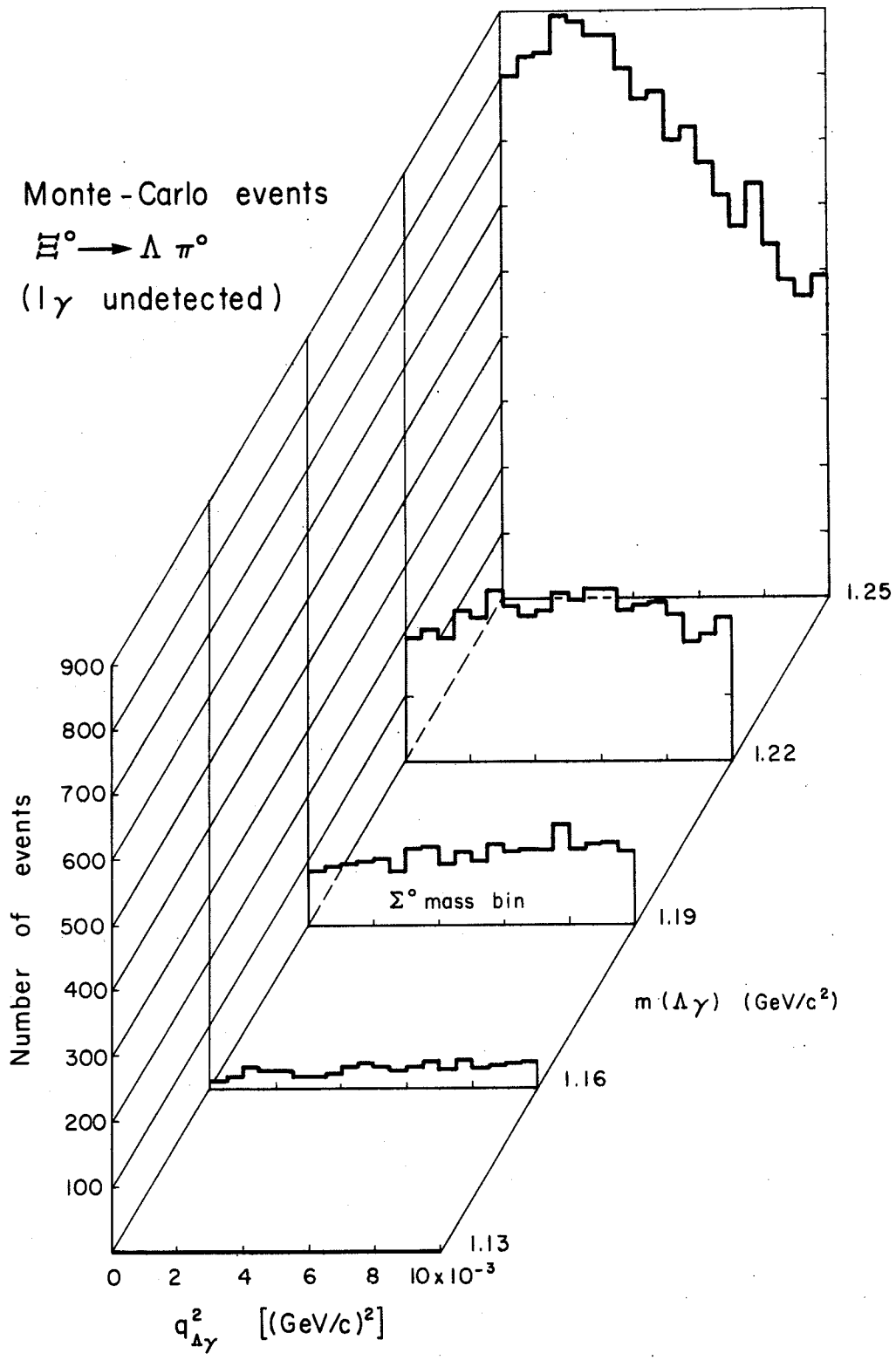
Monte-Carlo events
Ξ° → Λ π°
(1 γ undetected)
Number of events
900
800
700
600
500
400
300
200
100
Σ° mass bin
1.25
1.22
1.19
1.16
1.13
m (Λγ) (GeV/c²)
0
2
4
6
8
10x10⁻³
q²Λγ [(GeV/c)²]

Fig. 16

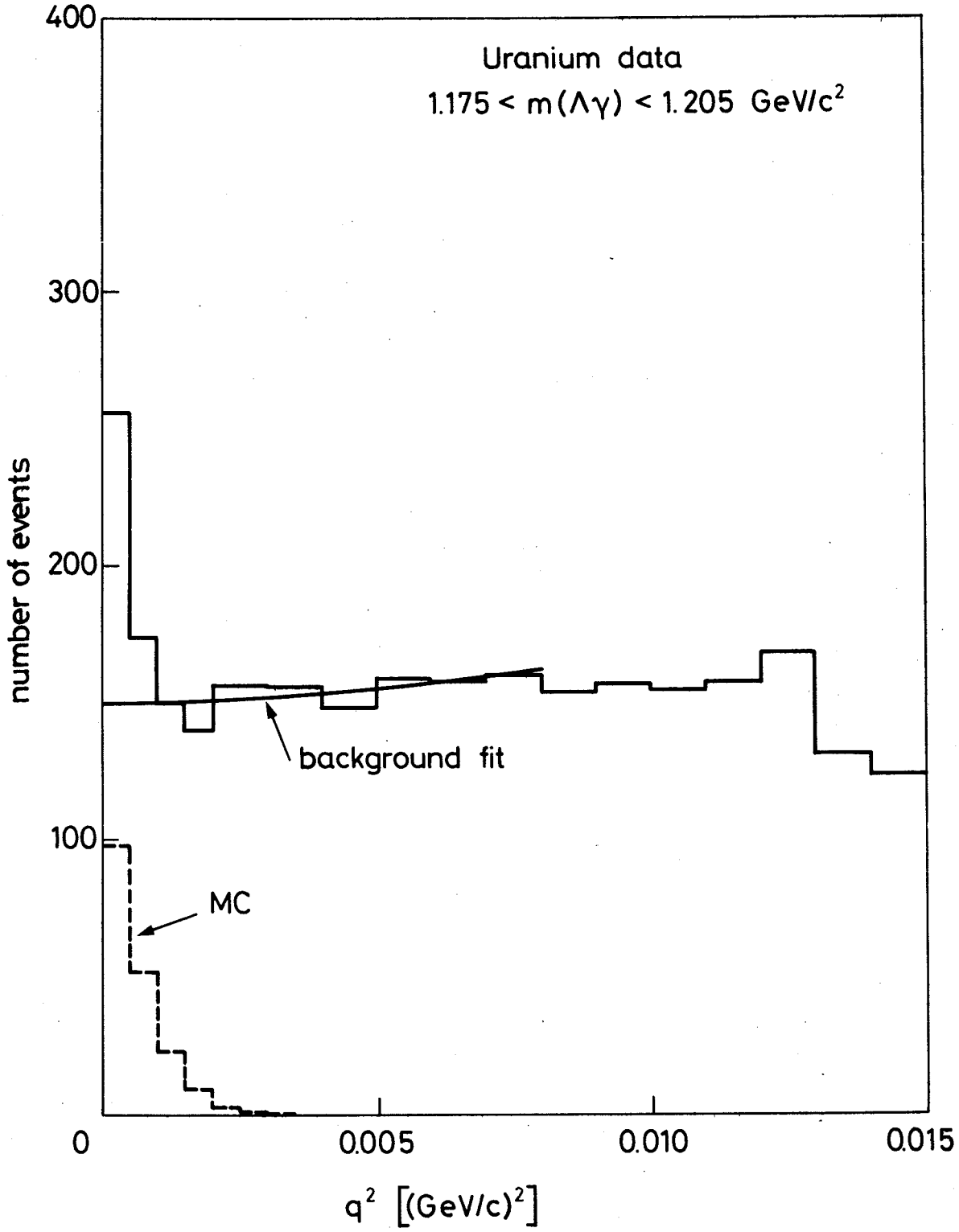
Uranium data
1.175 < m(Λγ) < 1.205 GeV/c²
number of events
400
300
200
100
0
0.005
0.010
0.015
background fit
MC
q² [(GeV/c)²]

Fig. 17

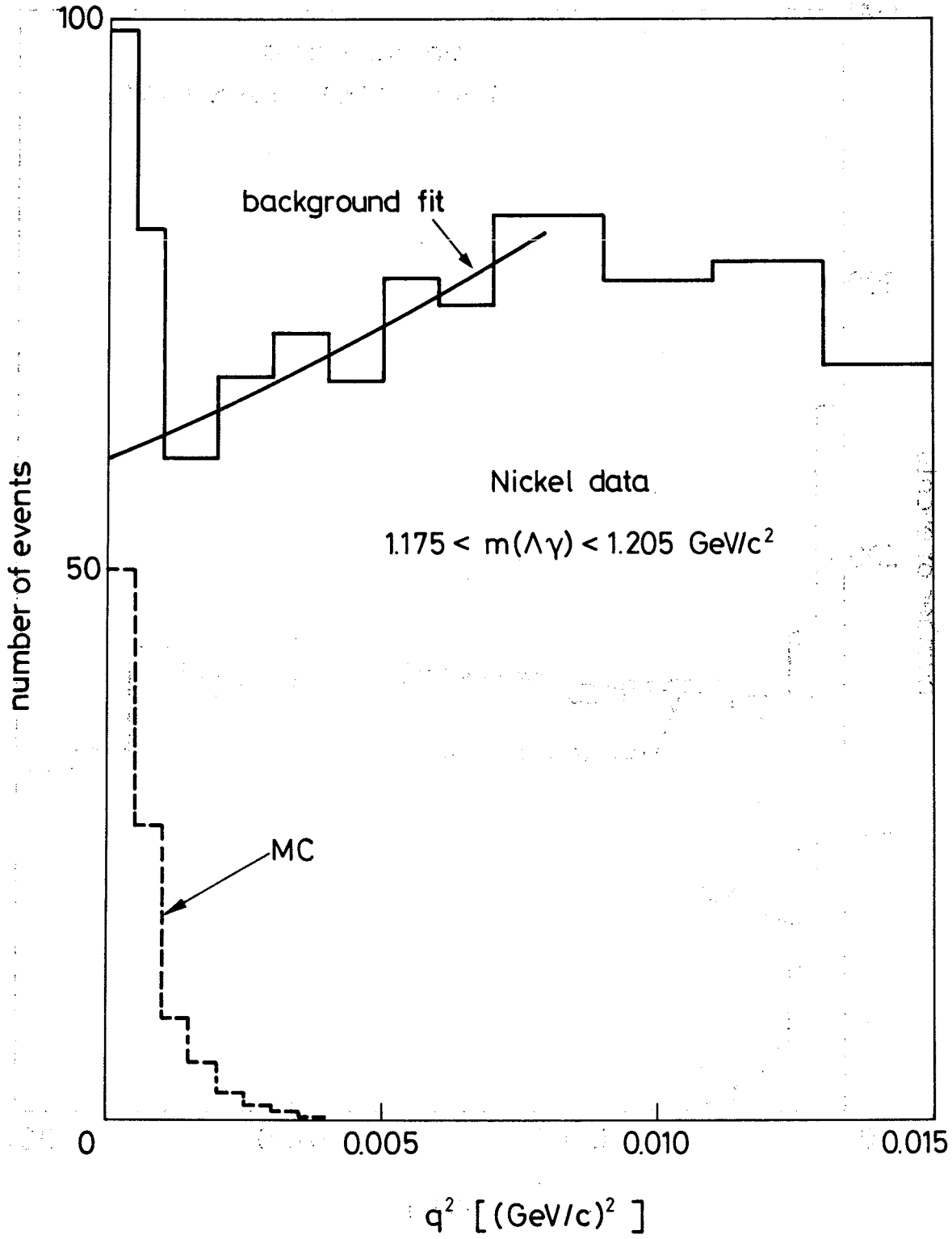
100
50
0
0.005
0.010
0.015
number of events
background fit
Nickel data
1.175 < m(Λγ) < 1.205 GeV/c²
MC
q² [(GeV/c)²]

Fig. 18

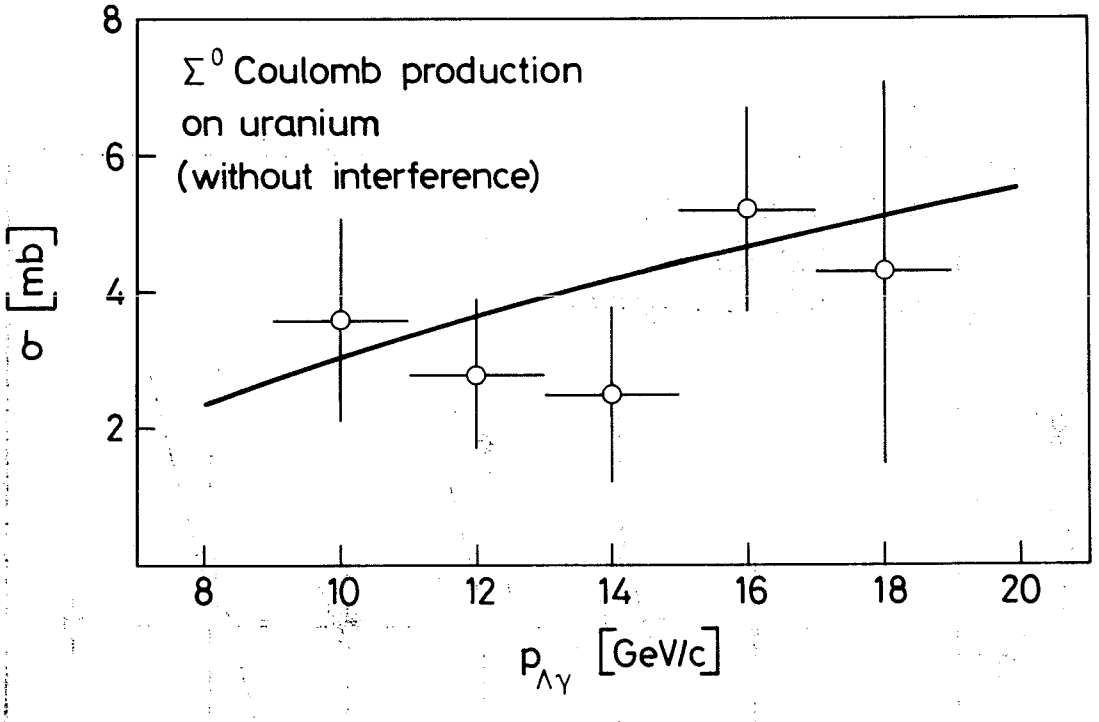

Fig. 19a

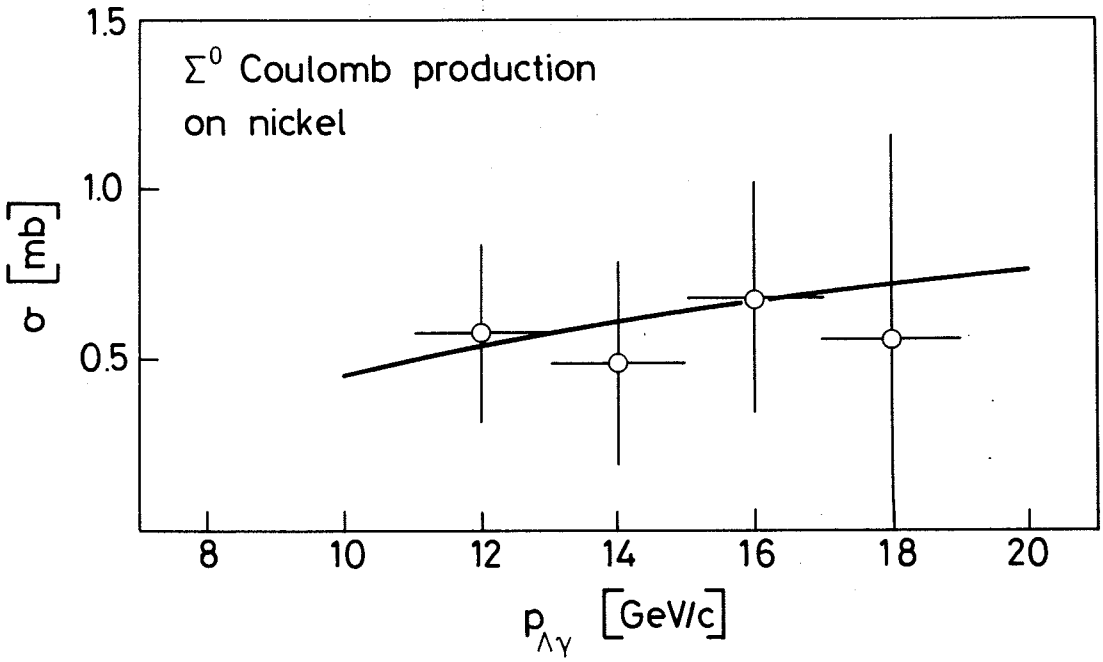

Fig. 19b

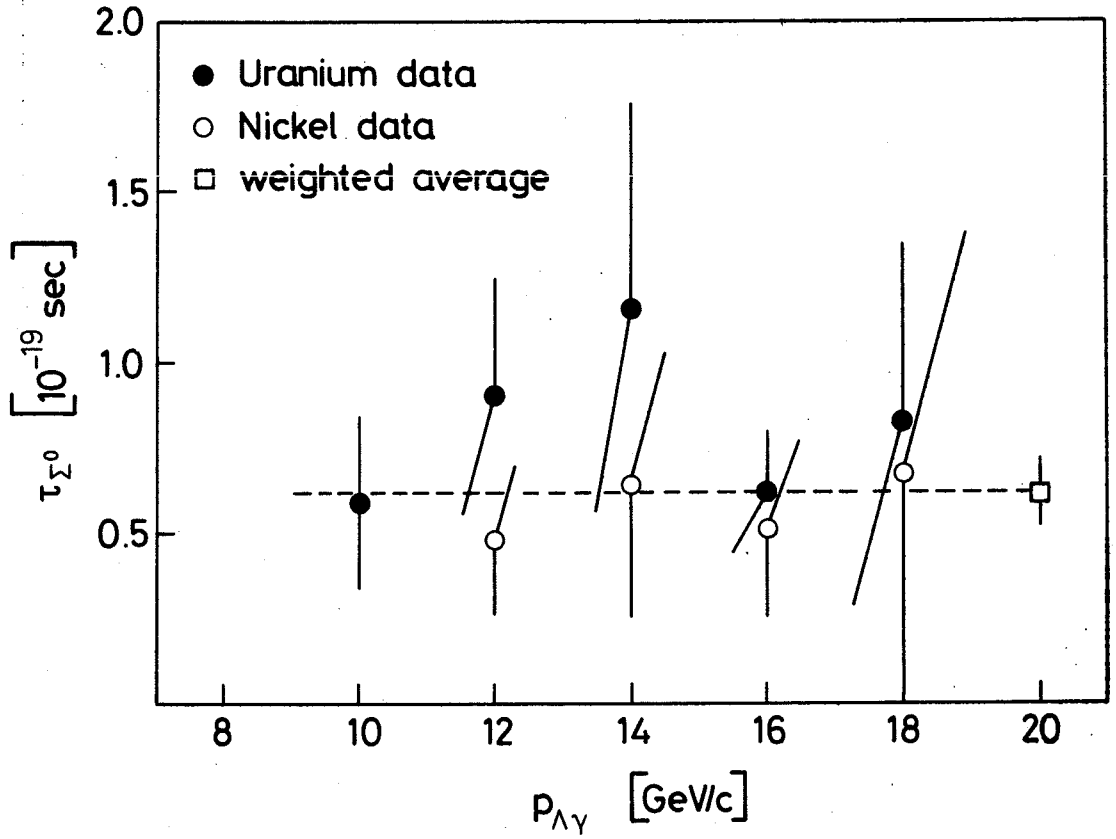
2.0
1.5
1.0
0.5
● Uranium data
○ Nickel data
□ weighted average
τ_{Σ^0} [10^{-19} sec]
8
10
12
14
16
18
20
$p_{\Lambda\gamma}$ [GeV/c]

Fig. 20